Icarus 397 (2023) 115507

Contents lists available at ScienceDirect

Icarus

journal homepage: www.elsevier.com/locate/icarus

Spectral effects of regolith porosity in the Mid-IR – Pyroxene

A.C. Martin [a,b,*], J.P. Emery [a], M.J. Loeffler [a,c]

[a] Department of Astronomy and Planetary Science, Northern Arizona University, Flagstaff, AZ 86011, United States of America
[b] Department of Physics, University of Central Florida, Orlando, Florida 32816, United States of America
[c] Center for Materials Interfaces in Research and Applications, Northern Arizona University, Flagstaff, AZ 86011, United States of America

ARTICLE INFO

Keywords:
Infrared observations
Spectroscopy
Experimental techniques
Regolith
Trojan asteroids

ABSTRACT

The regolith porosity on airless bodies in the Solar System has a known effect on remotely acquired spectra in the mid-infrared (MIR; 5–35 μm). Previous experiments quantifying this effect have focused on olivines. Here we report systematic laboratory experiments designed to quantify the effect of regolith porosity on the MIR spectra of pyroxene, an important rock forming mineral on Earth, the Moon, and throughout the Solar System. Specifically, we have measured MIR spectra of eight natural pyroxene minerals and mixtures over three particle size fractions (< 20 μm, 20–45 μm, and 45–63 μm) with varying degrees of porosity. Our results indicate that 0% regolith porosity spectra are dominated by surface scattering, 90% regolith porosity spectra are dominated by volume scattering, and the transition between the two regimes is gradual. Comparing selected spectra to the Trojan asteroid (624) Hektor, we estimate the regolith porosity of its surface to be >80%, and that the surface contains a significant fraction of amorphous material. Overall, these results are quite similar to our previous olivine findings, supporting the conclusion that regolith porosity strongly affects the shape and subsequent interpretation of MIR spectra of silicate-rich surfaces.

1. Introduction

Pyroxene is an important rock forming mineral on Earth, the Moon, throughout the Solar System, and beyond. Compositionally evolved asteroids form pyroxene via metamorphic and igneous processes, and this pyroxene can be detected with visible and near-infrared (VNIR; 0.5–2.5) spectroscopy (e.g., Klima et al., 2008; Sunshine et al., 2004). In particular, the pyroxenes low-calcium pigeonite, orthopyroxene, and high calcium augite are the most abundant mafic mineral in lunar mare basalts, while average eucrites (basaltic meteorites from Vesta) contain augite, pigeonite, and orthopyroxene (e.g., Delaney et al., 1984; Heiken et al., 1991). Pyroxene is also an important mineral that condenses out of the protoplanetary disk (Gail, 2004) and is present in chondrites (e.g., Dunn et al., 2010; Gastineau-Lyons et al., 2002) and primitive small bodies (e.g., comet 9P/Tempel 1; Lisse et al., 2006).

The pyroxene composition found on primitive small bodies can be indicative of Solar System formation region. Enstatite (the low-calcium, Mg-rich pyroxene endmember) is expected to form in the inner Solar System (e.g., Henning, 2010, and references therein). Mg-rich pyroxene (i.e., ferrosilite) can condense directly out of the early solar nebula if temperatures are high and oxygen fugacity (fO_2) is low (e.g., Petaev and Wood, 1998), and subsequent mixing within the disk can result in outer Solar System material containing a range of pyroxene Mg#s (i.e., Mg/(Mg + Fe)). For example, the dust from the coma of primitive small body, comet 81P/Wild 2, contained pyroxene with three distinct Mg# ranges that indicate different crystallization environments: 100–90, 90–75, and 75–50 (Frank et al., 2014). Additionally, Ultra-Carbonaceous Antarctic Meteorites (UCAMMs), which are thought to be cometary material (Wooden et al., 2017 and references therein), contain pyroxenes with a wide range of Mg#s (e.g., Dobrică et al., 2012). The commonality among pyroxenes sourced from primitive small bodies is a wide range of Mg#s that have been found associated with individual objects.

A large fraction of the primitive asteroid population are P- and D-type asteroids. These asteroids are spectrally featureless in the VNIR, but show spectral features indicative of anhydrous silicates in the mid-infrared (MIR; 5–35 μm). As shown in previous laboratory studies (Hamilton, 2000; Chihara et al., 2002), the location of some of the MIR spectral features change with Mg#, and thus could potentially be used to identify the composition of pyroxene present on an airless body, as well as where it may have formed (Gail, 2004; Henning, 2010).

One aspect that can potentially complicate the use of the MIR to

* Corresponding author.
E-mail address: Audrey.Martin@ucf.edu (A.C. Martin).

https://doi.org/10.1016/j.icarus.2023.115507
Received 23 November 2022; Received in revised form 27 February 2023; Accepted 5 March 2023
Available online 8 March 2023

extract the composition of a given pyroxene-rich asteroid is that the position of many absorption features may also depend on the porosity of the asteroid's regolith. Recently we have shown that changing the porosity of olivine powders, a somewhat simpler silicate than pyroxene, can cause the position of many of these MIR features to shift (Martin et al., 2022). Thus, in those studies we focused on determining which absorption features could be used to identify the Mg# regardless of the sample porosity. We also found that the spectral contrast of many other features depended on the particle size and sample porosity, which we interpreted as being an indicator of which scattering regime (surface vs. volume) was contributing to a given sample spectrum. Knowing the dominant scattering regime of a surface is important for estimating the porosity, and in turn, composition.

In this study, we turn our attention to studying the effect of porosity on the MIR of pyroxene powders. More specifically, we vary the porosity and particle size for a range of pyroxene compositions in order to quantitatively determine the degree to which these absorption features can be used to determine the composition of a pyroxene-rich airless body, regardless of its surface porosity. This work will allow us to bridge the gap between previous studies that focused solely on samples where surface scattering dominated (Hamilton, 2000) or where volume scatting dominated spectra (Chihara et al., 2002) and allow us to better interpret spectra obtain from a variety of airless bodies.

2. Spectral measurement

2.1. Sample suite

For our experiments, we purchased seven natural pyroxenes with differing compositions from Mineralogical Research Company and borrowed one sample from the American Museum of Natural History (Table 1). To verify mineralogy, pyroxene composition, and identify any potential contaminants, we used a Cameca SX-100 Electron Microprobe (EMP) at the University of Tennessee for petrological analysis. Because the samples are natural, many additional minor phases were identified and, for silicate phases, the Mg# was determined. The average ionic value from all EMP data for each sample are used to determine the Wo-En-Fs values (a pyroxene classification scheme that describes the ratio of Ca, Mg, and Fe in the M1 and M2 crystalline lattice site (see Hamilton (2000) for more discussion)).

2.2. Sample preparation and measurement

Once we determined the composition of the samples, we ground them with a mortar and pestle and removed all of the non-pyroxene phases. Next, we sieved them with a Gilson Performer III Sieve Shaker into three particle size ranges: 0–20 μm, 20–45 μm, and 45–63 μm. We note that the 20–45 μm and 45–63 μm samples were rinsed once with distilled water to remove clinging fines, but they were subsequently transported across the country without being rinsed a second time. As such, some mechanical breakdown of the particles may have occurred and produced additional clinging fines that were not removed. Once the pyroxene powders were ground and sieved, we mixed in KBr of the same particle size range. As KBr is transparent in the MIR, we use it as a proxy for porosity within the samples. KBr has been widely used for MIR spectral studies (e.g., Vernazza et al., 2012; Izawa et al., 2021). All pyroxene powder samples were mixed with KBr in ratios from 0% to 90% by weight, in 10 wt% intervals (Table 2). The balance precision (1 mg) dominates the uncertainties in the wt%, and is <0.5%. We use the term 'regolith porosity' to refer to the wt% of KBr in a sample mixture. Samples in the measuring sample cup have additional porosity from the volume of empty space (or void space) between particles, which we referred to as 'sample cup porosity'. The combined vol% of KBr and vol% of empty space is referred to as the 'total simulated porosity'.

After calculating the porosities, we took MIR measurements with a Thermo-Nicolet IS50 Fourier transform infrared (FTIR) spectrometer, under ambient temperature and pressure conditions, using the PIKE Technologies EasiDiff diffuse reflectance accessory. The reflected intensity (I_S) of the sample is an average of 200 scans between 4000 and 400 cm^{-1} at 4 cm^{-1} spectral resolution. To capture potential sample heterogeneity, we measure the reflected intensity of each sample twice, with the second measurement being done after rotating the sample cup ~90°, and took an average of the two measurements. For the reference spectrum, we measured the reflected intensity of pure KBr powder (I_{ref}) using the same particle size range as the target pyroxene mixture. The resulting reflectance spectrum (R) is I_s / I_{ref}, and was subtracted from 1 to convert to emissivity (E) following Kirchhoff's law (E = 1- R). We note that the correct application of Kirchhoff's law here would require measurements hemispherical reflectance. However, in applications to diffuse reflectance, as is measured here, the positions, shapes, or relative sizes of bands are not significantly affected (e.g., Salisbury et al., 1991). The error shown for the reflectance spectra is the standard deviation of the two sample spectra that were averaged, not the S/N of the measurement. The spectra of all minerals, particle size ranges, and regolith porosities are given in Figs. 1 through 8, and are discussed in more detail in Section 3.

3. Spectral analysis

For an agnostic analytical approach, we identify maxima (or peaks; P) and minima (or dips; D) in the spectra, as well as characterize the broad 10-μm plateau feature, using a feature-finding routine developed

Table 1
Compositional and locality information for all samples used in this study.

Sample Abrv.	Mineral	Mineral formula	Wo-En-Fs	Mg#	Possible additional phases	Locality
ENS	Enstatite	$MgSiO_3$	$Wo_{3.8}En_{86.2}Fs_{10}$	89.69 ± 1.32	≲5% Spinel/Chromite, Pigeonite (Mg_{88}), Diopside (Mg_{81})	Mirabel Springs, Mt. St. Helen, California
$DIOP_1$	Diopside	$MgCaSi_2O_6$	$Wo_{51.4}En_{46.6}Fs_{1.9}$	91.56 ± 1.37	<4% apatite, K-rich phyllosilicate, Fe-oxide, exsolved pyroxene	Outkumpo, Finland
$DIOP_2$	Diopside	$MgCaSi_2O_6$	$Wo_{50.68}En_{45.98}Fs_{3.33}$	92.81 ± 1.26	≲4% Quartz, Augite (Mg_{91}), Pigeonite (Mg_{93}), Enstatite (Mg_{96})	Route 16 Road cut, Little Moose, Maine
HEN_1	Hedenbergite	$CaFeSi_2O_6$	$Wo_{57.0}En_{2.9}Fs_{40.1}$	6.74 ± 0.15	Trace Fe-Oxide	Lanzi Mine, Livorno Providence, Italy
HEN_2	Hedenbergite	$CaFeSi_2O_6$	$Wo_{60.8}En_{4.6}Fs_{34.5}$	11.87 ± 1.15	Trace Ca inclusion, Fe-oxide	Dal'negrosk, Kavalerovo mining district, Russia
AEG	Aegirine	$NaFeSi_2O_6$	$Wo_{19.76}En_{8.95}Fs_{71.29}$	1.92 ± 0.15	N/A	Mt. Malosa, Zomba District, Malawi
AUG	Augite	$(Ca,Mg,Fe,Na)(Mg,Fe,Al)(Si,Al)_2O_6$	$Wo_{98.97}En_{0.10}Fs_{0.93}$	6.57 ± 10.66	≲8% Phlogopite, Fe/Ti-oxide, Quartz, Enstatite (Mg_{51}), Hypersthene/Pigeonite (Mg_{43})	Jacurpiranga Mine, Sao Paulo, Brazil
MXT	Fayalite/ Enstatite	$(Mg,Fe)_2SiO_4$/ $MgSiO_3$	$Wo_{5.36}En_{54.77}Fs_{39.87}$	44.80 ± 0.52/ 56.75 ± 1.68	~10% Augite (Mg_{65}), pigeonite (Mg_{59}). Trace albite, anorthosite	Bushveld, South Africa (B06–045)

Table 2
The weight percent of KBr in a sample (Regolith Porosity; units in wt%), the percent volumetric contribution of air to the empty space in a sample cup (Sample Cup Porosity; units in vol%), and the combined percent volumetric contribution of air and KBr in a sample cup (Total Simulated Porosity; units in vol%) are listed above for each sample for all three particle sizes. Each sample suite is listed from a target of 0% regolith porosity (top) to 90% regolith porosity (bottom) in 10% increments.

Sample	Regolith porosity (wt% KBr)			Sample cup porosity (vol% air)			Total simulated porosity (vol% air + KBr)		
	0–20 μm	20–45 μm	45–63 μm	0–20 μm	20–45 μm	45–63 μm	0–20 μm	20–45 μm	45–63 μm
ENS	0.00	0.00	0.00	70.30	60.90	63.67	70.30	60.90	63.67
	10.84	10.00	10.89	76.68	57.69	50.79	80.41	63.32	57.53
	20.69	20.00	19.80	74.21	56.86	51.58	81.20	67.95	63.99
	30.69	29.70	30.05	72.32	53.18	48.06	83.81	69.89	64.73
	40.30	39.41	39.60	64.96	51.98	51.33	80.38	74.47	73.30
	50.25	50.00	50.49	64.99	52.69	48.40	83.91	79.62	76.40
	60.20	60.00	59.41	65.41	50.21	48.10	87.47	83.97	80.09
	69.31	69.95	70.44	63.60	50.08	51.15	89.96	87.75	87.95
	78.82	80.10	79.41	64.06	50.59	46.78	93.26	92.44	90.19
	90.00	90.15	89.60	63.48	49.81	50.10	96.82	96.19	95.48
$DIOP_1$	0.00	0.00	0.00	77.90	70.53	62.71	77.90	70.53	62.71
	11.33	9.93	10.75	79.94	70.17	65.61	82.68	73.75	70.06
	20.40	20.46	19.93	78.15	69.62	61.13	83.41	76.95	70.28
	30.20	30.10	30.56	78.54	70.35	62.47	86.02	80.65	75.69
	39.80	40.53	39.54	77.02	68.96	59.94	87.36	83.15	77.85
	50.25	49.68	50.17	74.13	67.25	59.93	88.50	85.25	82.15
	60.20	60.53	59.87	72.85	66.31	58.18	90.54	88.37	85.30
	69.65	69.64	70.20	74.21	64.54	58.62	93.28	90.76	89.42
	79.31	79.61	79.41	71.77	63.63	58.04	95.08	93.76	92.73
	90.00	89.11	89.47	71.17	64.52	58.58	97.62	96.81	96.40
$DIOP_2$	0.00	0.00	0.00	74.60	68.25	58.81	74.60	68.25	58.81
	10.45	9.93	10.55	72.30	69.17	58.11	75.80	72.87	63.45
	20.00	19.80	20.07	71.52	66.25	57.36	78.25	74.15	67.46
	30.50	30.00	30.26	70.67	66.52	56.73	80.99	78.12	71.84
	41.38	40.47	39.60	71.58	58.26	55.66	84.82	77.32	75.51
	49.75	49.49	50.32	68.34	55.08	54.64	85.77	79.69	79.86
	60.39	60.06	60.20	65.77	65.97	55.55	88.13	88.10	84.51
	69.65	70.07	68.85	66.63	64.32	57.78	91.30	90.84	88.69
	80.00	79.15	79.74	67.47	55.35	53.95	94.53	92.16	92.15
	89.71	89.77	88.89	64.87	56.18	56.26	97.02	96.30	95.98
HEN_1	0.00	0.00	0.00	76.45	72.24	63.20	76.45	72.24	63.20
	9.95	9.90	10.00	69.89	64.77	59.64	73.65	69.14	64.67
	20.40	20.79	20.69	75.06	68.30	55.15	81.26	76.33	66.30
	29.76	29.85	30.35	74.08	58.04	56.70	83.24	72.92	72.01
	39.90	40.00	40.89	73.89	54.82	52.05	85.94	75.72	74.18
	49.75	50.00	49.75	72.15	52.21	57.95	87.78	79.14	81.54
	58.94	60.40	59.61	70.77	53.15	57.69	89.75	84.22	85.17
	69.95	69.76	69.05	71.10	55.81	54.29	92.78	88.89	88.59
	79.50	80.20	79.41	71.01	53.16	53.23	95.17	92.48	92.21
	89.55	90.00	89.27	70.12	55.22	52.12	97.52	96.45	96.03
HEN_2	0.00	0.00	0.00	74.89	63.35	57.74	74.89	63.35	57.74
	11.04	10.26	9.85	73.69	58.89	56.54	76.95	64.18	62.54
	20.26	20.85	20.20	72.59	59.31	56.41	79.34	69.64	67.17
	30.29	30.03	30.20	71.16	58.63	55.20	81.50	73.38	71.30
	40.66	39.93	40.89	72.26	57.88	56.75	85.34	77.33	77.05
	49.67	50.82	50.24	70.87	57.58	55.02	87.35	81.82	80.22
	60.07	60.13	59.61	70.17	55.11	54.94	89.73	84.77	84.68
	69.71	69.93	69.46	69.63	58.34	54.61	92.28	89.59	88.57
	79.67	79.08	79.80	70.03	54.73	56.78	95.09	92.30	92.87
	89.84	89.70	90.00	65.57	57.33	58.10	97.27	96.51	96.63
AEG	0.00	0.00	0.00	71.53	67.76	59.58	71.53	67.76	59.58
	11.17	10.29	9.80	70.97	62.95	60.57	74.99	67.69	65.39
	20.10	19.80	18.47	67.94	59.50	55.84	75.75	69.23	65.76
	29.56	30.20	29.56	68.33	61.11	61.01	79.39	74.97	74.63
	40.10	40.59	40.49	65.01	60.07	57.63	81.16	78.70	77.35
	50.50	50.50	50.00	66.97	60.51	59.48	85.67	82.87	82.23
	59.42	59.51	60.40	66.25	59.09	59.18	88.26	85.80	86.17
	69.31	69.80	69.61	64.88	58.64	55.65	90.97	89.55	88.72
	79.90	79.60	79.90	64.59	57.11	58.62	94.18	92.85	93.20
	88.35	88.41	88.52	63.90	58.21	56.63	96.63	96.12	96.01
AUG	0.00	0.00	0.00	74.60	63.53	61.74	74.60	63.53	61.74
	10.78	10.82	11.04	72.78	68.44	60.24	76.32	72.56	65.53
	20.30	20.66	20.27	71.85	58.50	58.03	78.59	68.61	68.06
	30.58	30.07	30.03	68.92	57.27	57.80	79.88	72.10	72.43
	39.90	40.13	39.93	69.00	60.25	60.62	82.97	78.26	78.39
	50.25	49.50	49.67	69.94	56.90	56.34	86.63	80.51	80.33
	60.00	60.13	60.00	69.88	59.27	56.31	89.45	85.78	84.70
	69.65	69.97	69.41	68.71	57.69	55.46	91.85	89.10	88.29
	79.70	79.54	79.54	70.40	56.87	56.67	94.94	92.57	92.54
	89.76	86.42	89.44	67.44	52.75	95.94	97.25	94.67	95.94
MXT	0.00	0.00	0.00	72.08	62.85	47.06	72.08	62.85	47.06

(*continued on next page*)

Table 2 (*continued*)

Sample	Regolith porosity (wt% KBr)			Sample cup porosity (vol% air)			Total simulated porosity (vol% air + KBr)		
	0–20 μm	20–45 μm	45–63 μm	0–20 μm	20–45 μm	45–63 μm	0–20 μm	20–45 μm	45–63 μm
	10.00	10.00	10.00	71.62	55.31	48.06	75.39	61.26	54.98
	20.00	20.00	20.00	73.67	57.41	53.04	80.54	68.40	65.10
	30.00	30.00	30.00	77.94	57.85	54.62	86.20	73.55	71.50
	40.00	40.00	40.00	81.70	58.43	56.41	90.47	78.36	77.31
	50.00	50.00	50.00	80.22	59.13	57.74	91.70	82.84	82.26
	60.00	60.00	60.00	80.13	57.10	59.96	93.53	86.04	86.97
	69.77	69.95	70.00	77.15	63.14	62.40	94.59	91.27	91.10
	79.65	79.88	80.00	82.88	67.35	62.79	97.38	95.00	94.30
	90.00	90.00	90.00	76.55	64.83	63.26	98.25	97.38	97.27

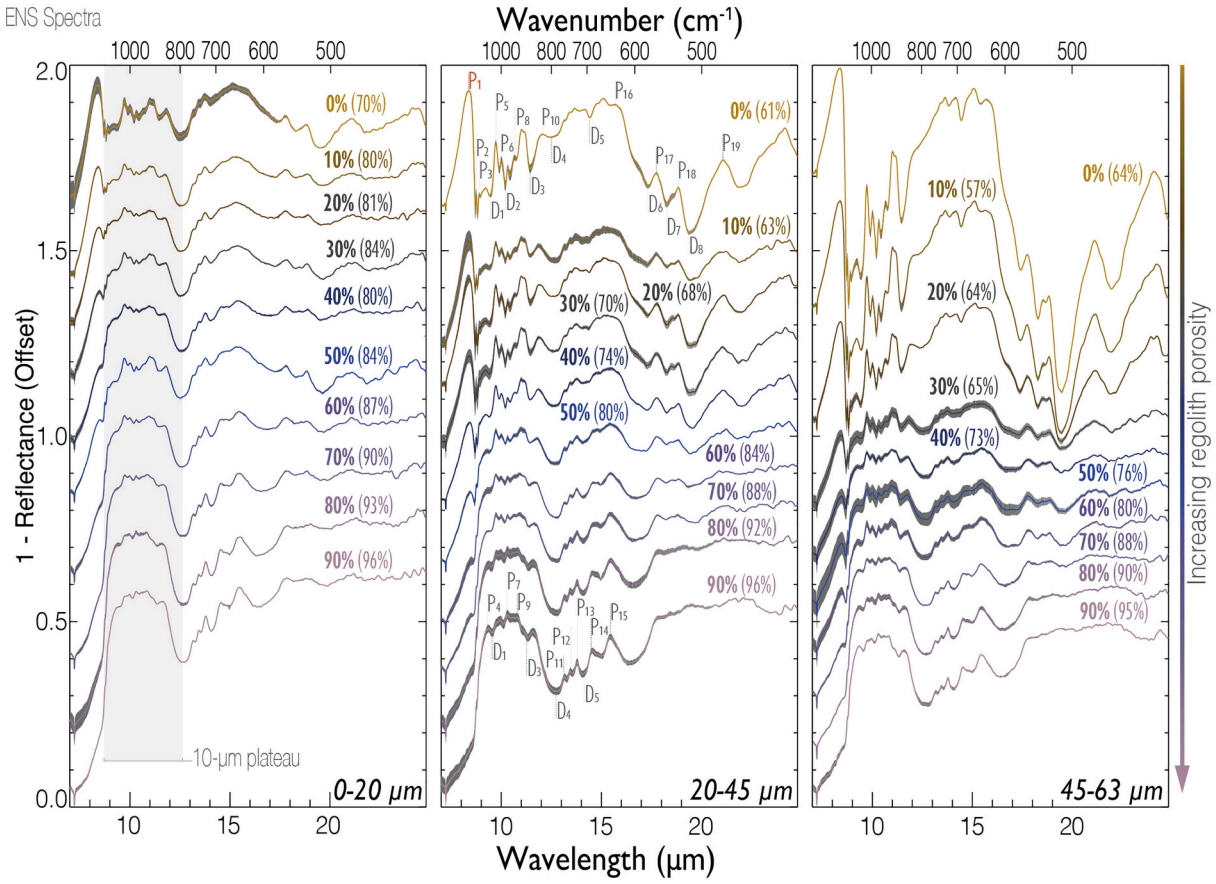

Fig. 1. Spectra of ENS powder mixed with increasing wt% of KBr (from top to bottom) to represent regolith porosity. Gray region around the spectral curve represents standard deviation between each measurement of a given samples (i.e., sample heterogeneity). Bold percentages listed for each spectra represent the weight percent of KBr, while the percentages in parentheses are total simulated porosity (units of vol%). Each panel contains a different range of particle sizes (from left to right: 0–20, 20–45, and 45–63 μm). Spectra have been vertically offset for clarity and features are labeled in the 20–45 μm panel. The 20–45 μm spectral plot shows maxima labeled with 'P' and minima labeled with 'D'. The CF_1 (P_1) is labeled in red. The approximate 10-μm plateau region is shaded slightly in the 0–20 μm plot. (For interpretation of the references to colour in this figure legend, the reader is referred to the web version of this article.)

in our previous work (Martin et al., 2022). We note that although some of these features correspond to bands (reststrahlen or vibrational), not all do. Key spectral parameters that we extract to help us quantify the effect of regolith porosity are features' position, width, and spectral contrast, the latter of which is defined as the height (or depth) of a feature above (or below) the continuum (see Martin et al., 2022, Section 4.1.1. for a detailed description of parameter definitions).

The most prominent, independent feature trends we found with respect to regolith porosity are the peak position and spectral contrast of some key features (discussed below). Table 3 lists all the features whose spectral contrast positively and negatively trend with regolith porosity. In addition to position and spectral contrast, we investigated the base width and FWHM of each feature. Though some trends are present, they are largely insignificant. We also explored all feature parameters as a function of the other feature parameters (e.g., spectral contrast vs. feature position). A few weak relationships may be present; however, we do not find them significant. All parameter values can be found in supplemental material.

In the following sections we describe the spectra, individual features, 10-μm plateau, and parameters we use to assess the spectral effects of regolith porosity of each sample. For clarity, we refer to the spectrum of sample PYX_a, with a particle size fraction 'b', and regolith porosity of 'c' as $PYX_{a,b,c}$. Particle size fractions will be referred to in terms of S (0–20 μm), M (20–45 μm), and/or L (45–63 μm). For example, the spectrum of sample HEN_2, with 0–20 μm particle size fraction, and 80% regolith porosity is '$HEN_{2,S,80}$', and the spectrum of sample ENS, in all particle

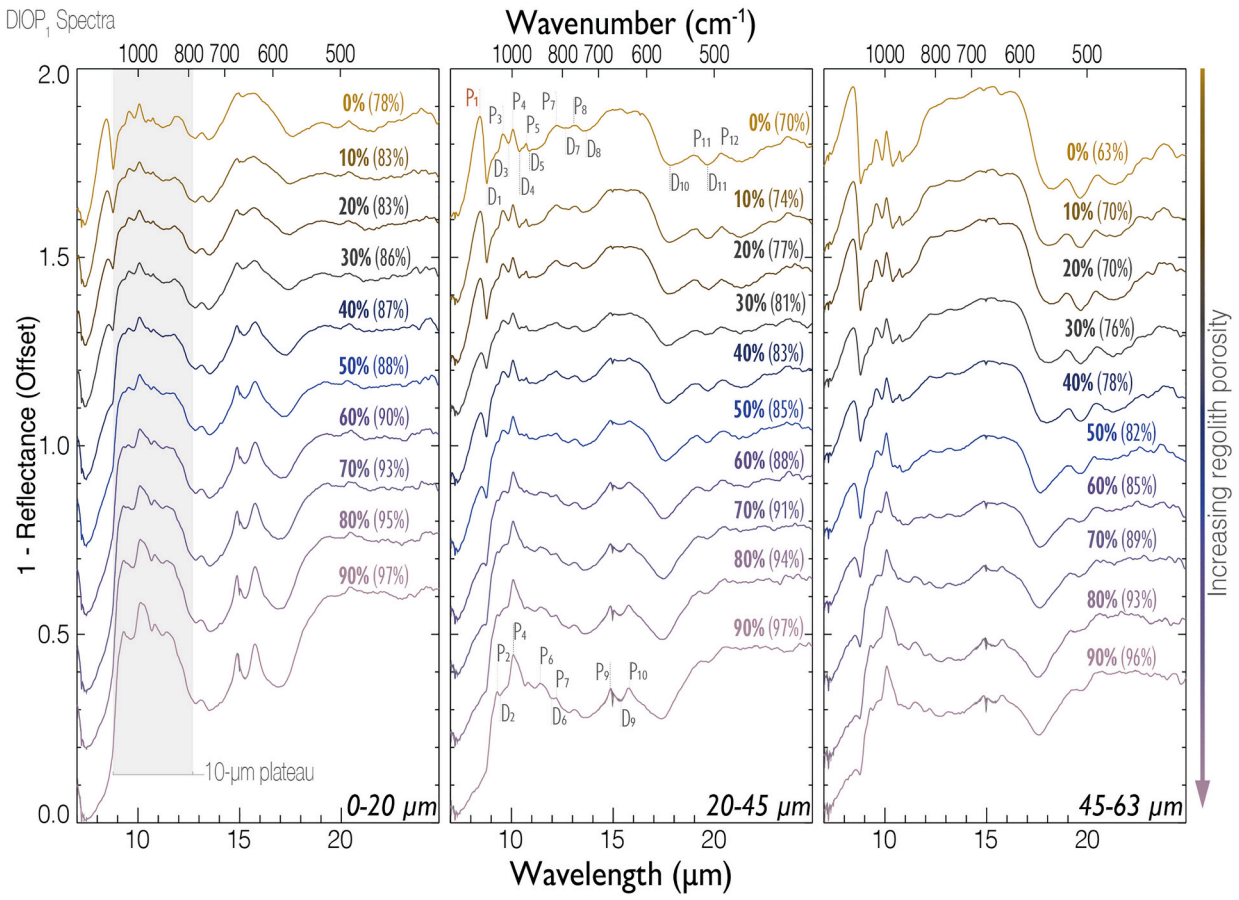

Fig. 2. .Spectra of $DIOP_1$ powder mixed with increasing wt% of KBr (from top to bottom) to represent regolith porosity. Gray region around the spectral curve represents standard deviation between each measurement of a given samples (i.e., sample heterogeneity). Bold percentages listed for each spectra represent the weight percent of KBr, while the percentages in parentheses are total simulated porosity (units of vol%). Each panel contains a different range of particle sizes (from left to right: 0–20, 20–45, and 45–63 μm). Spectra have been vertically offset for clarity and features are labeled in the 20–45 μm panel. The 20–45 μm spectral plot shows maxima labeled with 'P' and minima labeled with 'D'. The CF_1 (P_1) is labeled in red. The approximate 10-μm plateau region is shaded slightly in the 0–20 μm plot. (For interpretation of the references to colour in this figure legend, the reader is referred to the web version of this article.)

size fractions, and regolith porosity from 0 to 50% is '$ENS_{SML,0–50}$'. Additionally, each spectral suite has a different set of composite features, which will be defined below.

3.1. Enstatite

The 0% regolith porosity spectra of enstatite (ENS) samples strongly resemble one another (Fig. 1), though there are distinct differences between each particle size spectral suite, primarily related to spectral contrast. All of the $ENS_{SML,0}$ spectra have a prominent maximum at ~8.4 μm (P_1) that likely correspond to the Christiansen Feature (CF_1). However, the spectral contrast of CF_1 in $ENS_{S,0}$ is ~22%, while the spectral contrast of ~38% in $ENS_{L,0}$. Between the CF_1 and ~12.5 μm feature (marked by D_4 in $ENS_{S,0}$ and P_{10} in $ENS_{ML,0}$), each spectrum exhibits a series of sharp maxima and minima. At longer wavelengths the spectra have a series of three minima around 17.0 μm, 18.3, and 19.6 μm (D_6, D_7, and D_8 respectively). When the three minima overlap the spectral contrast is much larger in $ENS_{ML,0}$ (~140%) compared to $ENS_{S,0}$ (~94%).

As regolith porosity increases, the series of sharp features within the 10-μm region shallow and a large minimum around 12.55 μm (D_4) deepens. This minimum is present for spectra of all $ENS_{S,0–90}$ spectra, but only starts to take shape in $ENS_{L,0–90}$ when regolith porosity reaches ~30%. Additionally, three step-like maxima at ~13.16 μm, 13.46 μm, and 13.75 μm (P_{11}, P_{12}, and P_{13} respectively) appear in all $ENS_{S,0–90}$ spectra and most of $ENS_{M,0–90}$ spectra, but only begin to be resolved in $ENS_{L,0–90}$ spectra near 30–40% regolith porosity. Finally, all $ENS_{SML,70–90}$ show a 10-μm plateau with very similar spectral contrast.

3.2. Diopsides

The spectra of both diopside samples ($DIOP_1$ and $DIOP_2$) strongly resemble one another at each particle size studied (Figs. 2 and 3). In $DIOP_{1,SML,0}$ and $DIOP_{2,SML,0}$ common features include a large maximum at ~8.5 μm (P_1) that corresponds to CF_1 followed by a deep minimum at ~8.78 μm (D_1) that likely corresponds to a reststrahlen band (RB; absorption features associated with Si—O fundamental stretching and bending). $DIOP_{1,SML,0}$ has a double maximum that resembles another double-peaked feature around 10.14 μm ($P_{3/4}$), whereas $DIOP_{2,SML,0}$ has a high spectral contrast trapezoidal feature with a shoulder on the short wavelength side and a maximum near 10.02 μm (P_4) on the long wavelength side. Both spectral suites exhibit a wide bowl-shaped minimum between P_4 and P_7, when the regolith porosity is low (≲40%), consisting of two minima at ~10.5 μm (D_4) and ~11.0 μm (D_5) for $DIOP_{1,SML,0–40}$, and ~10.5 μm (D_2) and ~11.0 μm (D_3) for $DIOP_{2,SML,0–40}$. This bowl-shaped feature is much shallower in $DIOP_{1,S,0–40}$ and $DIOP_{2,S,0–40}$ than in spectra of larger particles. Finally, both spectral suites have a deep minimum around 17.5 μm (D_{10} for $DIOP_{1,SML,0}$ and D_7 for $DIOP_{2,SML,0}$), followed by a shallower minimum around 19.6 μm (D_{11} for $DIOP_{1,SML,0}$ and D_8 for $DIOP_{2,SML,0}$).

Spectral characteristics of the features change significantly as KBr is added to the mixture, and the changes are consistent between the two

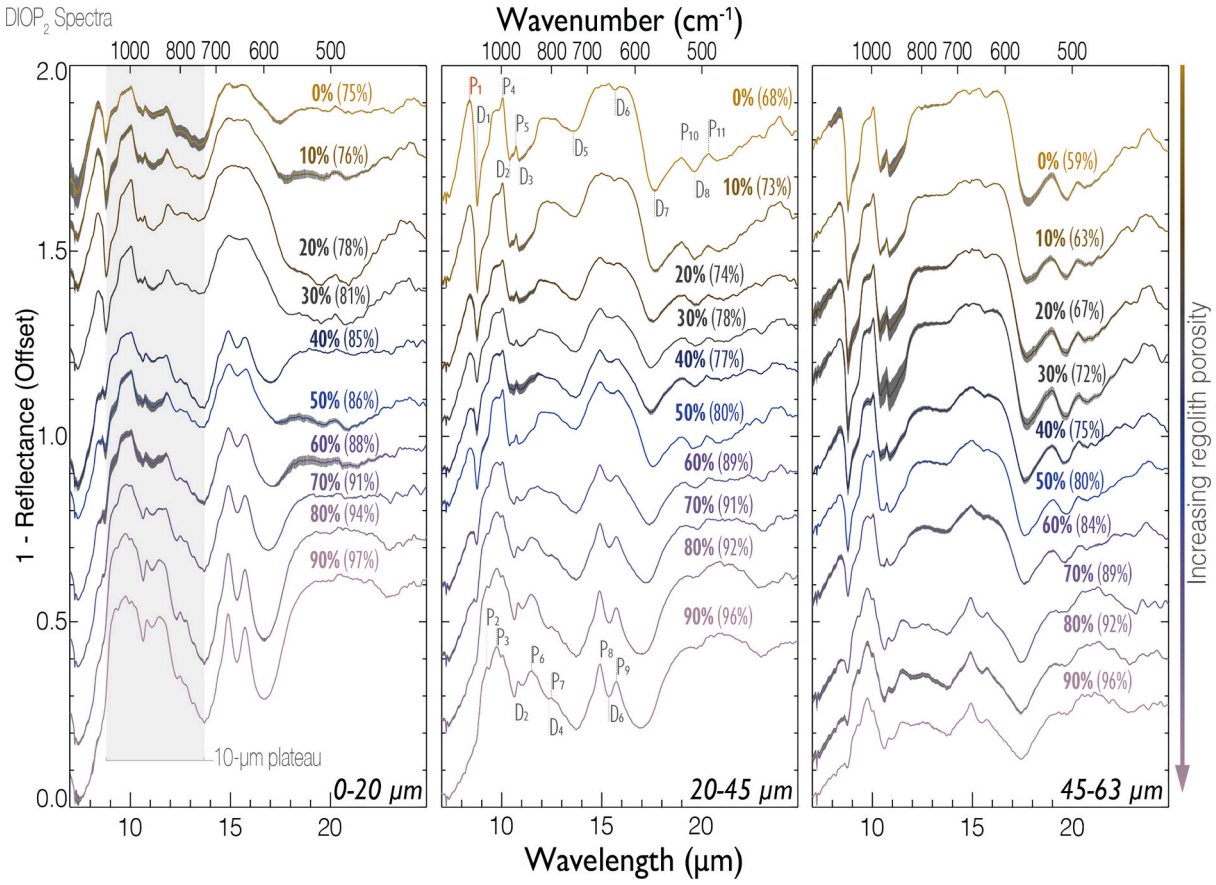

Fig. 3. Spectra of $DIOP_2$ powder mixed with increasing wt% of KBr (from top to bottom) to represent regolith porosity. Gray region around the spectral curve represents standard deviation between each measurement of a given samples (i.e., sample heterogeneity). Bold percentages listed for each spectra represent the weight percent of KBr, while the percentages in parentheses are total simulated porosity (units of vol%). Each panel contains a different range of particle sizes (from left to right: 0–20, 20–45, and 45–63 μm). Spectra have been vertically offset for clarity and features are labeled in the 20–45 μm panel. The 20–45 μm spectral plot shows maxima labeled with 'P' and minima labeled with 'D'. The CF_1 (P_1) is labeled in red. The approximate 10-μm plateau region is shaded slightly in the 0–20 μm plot. (For interpretation of the references to colour in this figure legend, the reader is referred to the web version of this article.)

diopside spectral suites. The spectral contrast of CF_1 (P_1) decreases from ~20% to 0% as the regolith porosity increases. The $DIOP_{1,S,0}$ double maxima near 10.14 μm gradually becomes a single peak at ~10.10 μm (P_4) around 60% regolith porosity, and a $DIOP_{2,S,0}$ trapezoidal feature in the same location also transforms into a single maximum at ~9.77 μm (P_3) around 70% regolith porosity. $DIOP_{1,L,0–90}$ and $DIOP_{2,L,0–90}$ show $D_{4/5}$ ($DIOP_1$) and $D_{2/3}$ ($DIOP_2$) decreasing in spectral contrast, but the decrease is less than occurs in the spectra of samples with smaller particle sizes. As such, the 10-μm plateau that forms at high regolith porosities is suppressed in $DIOP_{1,L,0–90}$ and $DIOP_{2,L,0–90}$. The spectral contrast of the bowl-shaped feature decreases and a minimum near 13.5 μm (D_8 and D_5 for $DIOP_{1,SML,0–90}$ and $DIOP_{2,SML,0–90}$ respectively) deepens as regolith porosity increases. The broad maxima/plateau on the long wavelength side of this minimum present at 0% regolith porosity gradually becomes a distinct double maximum ($P_{9/10}$ and $P_{8/9}$ for $DIOP_{1,SML,0–90}$ and $DIOP_{2,SML,0–90}$ respectively). This double maximum has much larger spectral contrast in the spectra of smaller particle sized samples (~25% in $DIOP_{1,S,90}$ and ~ 55% in $DIOP_{2,S,90}$) than in larger particle size samples (~16% in $DIOP_{1,L,90}$ and ~ 27% in in $DIOP_{2,L,90}$).

3.3. Hedenbergites

The spectra of both hedenbergite samples (HEN_1 and HEN_2) strongly resemble one another for each particle size studied (Figs. 4 and 5). Common features found in both $HEN_{1,SML,0}$ and $HEN_{2,SML,0}$ include a large maximum at ~8.5 μm (P_1) that corresponds to the CF_1, followed by a deep minimum at ~8.8 μm (D_1) that likely corresponds to an RB, a minimum around ~13.8 μm (D_5) that is deeper for smaller particle sizes and likely corresponds to the transparency feature (TF; regions of low absorption coefficients) TF, and a minimum near ~17.5 μm (D_7) that is deeper for larger particles.

The spectral characteristics of many features change significantly as more KBr is added to the mixture (i.e., increasing regolith porosity). For instance, the spectral contrast of CF_1 (P_1) decreases from ~20% to 0% as the regolith porosity increases. Double maxima at ~10.0 μm (P_3 and P_4) separate until P_3 disappears in $HEN_{1/2,S,30}$, and a minimum (D_2) widens between a newly appearing maximum (P_2) and P_4.

The 10-μm plateau, which extends between 8 and 14 μm, appears to be composed of three maxima in spectra of higher porosity samples (P_2 and two double maximum; $P_{4/5}$ and $P_{6/7}$). In $HEN_{1,S,0–90}$ spectra, the three maxima become apparent at ~50% regolith porosity, while in $HEN_{1,ML,0–90}$ spectra they become apparent at ~70% regolith porosity. In $HEN_{2,L,0–90}$, the three maxima that make up the 10-μm plateau do not appear at all. The spectral contrast of the $HEN_{1/2,S,90}$ 10-μm plateau is ~135%, but ~120% in $HEN_{1,L,90}$ and 50% in $HEN_{2,L,90}$. Finally, a broad maximum at ~16.0 μm shallows and resolves into a minimum (D_6) between two maxima (P_8 and P_9 for HEN_1; P_9 and P_{10} for HEN_2) as the regolith porosity increases.

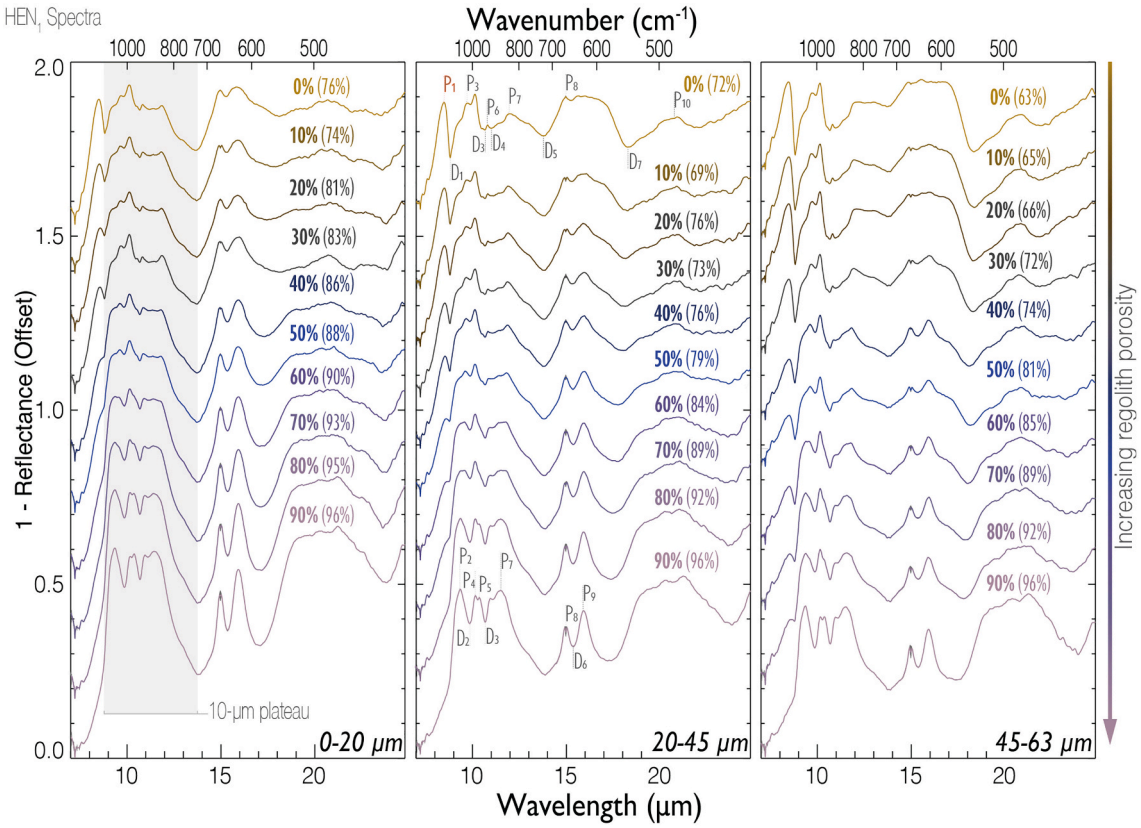

Fig. 4. Spectra of HEN_1 powder mixed with increasing wt% of KBr (from top to bottom) to represent regolith porosity. Gray region around the spectral curve represents standard deviation between each measurement of a given samples (i.e., sample heterogeneity). Bold percentages listed for each spectra represent the weight percent of KBr, while the percentages in parentheses are total simulated porosity (units of vol%). Each panel contains a different range of particle sizes (from left to right: 0–20, 20–45, and 45–63 μm). Spectra have been vertically offset for clarity and features are labeled in the 20–45 μm panel. The 20–45 μm spectral plot shows maxima labeled with 'P' and minima labeled with 'D'. The CF_1 (P_1) is labeled in red. The approximate 10-μm plateau region is shaded slightly in the 0–20 μm plot. (For interpretation of the references to colour in this figure legend, the reader is referred to the web version of this article.)

3.4. Aegirine

Characteristics of $AEG_{ML,0}$ are similar to each other, while $AEG_{S,0}$ is distinctly different (Fig. 6). Both $AEG_{ML,0}$ exhibit a prominent maximum at ~8.3 μm (P_2) that corresponds to the CF_1, a sharp minimum at ~8.6 μm (D_1), followed by two sharp maxima at ~9.0 μm (P_3) and ~9.7 μm (P_4). All $AEG_{SML,0}$ contain a broad hump near 11.6 μm (P_6), followed by a minimum at 13.0 μm (D_5) that likely corresponds to the TF, then a sharp maximum 13.6 μm (P_7). The shape of P_8 in $AEG_{S,0}$ is slightly broader than in $AEG_{ML,0}$. In $AEG_{ML,0}$, P_8 is followed by a shoulder-like feature (P_9) that forms a trapezoidal-like plateau. There is a steep dive into a series of maxima and minima in the 16.5–19.0 μm region. As the regolith porosity increases, P_2 shrinks until it disappears altogether, while the deep minima found in $AEG_{ML,0}$ shallow (D_7, D_8, D_9), and P_8 grows. All $AEG_{SML,90}$ exhibit a 10-μm plateau. The plateau has a higher maximum spectral contrast in $AEG_{S,90}$ (~140%) compared to $AEG_{ML,90}$ (~80%), and the spectral contrast increases with an increasing amount of KBr.

3.5. Augite

There are spectral similarities in augite medium and large particle size spectra, $AUG_{ML,0}$, while $AUG_{S,0}$ is distinctly different (Fig. 7). Both $AUG_{ML,0}$ exhibit a prominent maximum at ~8.1 μm (P_1) that corresponds to the CF_1, a minimum at ~9.5 μm (D_2), and a trapezoidal pyramid feature from ~10.9 μm (P_4) to ~18.3 μm (D_6), while $AUG_{S,0}$ contains a small maximum (P_1), followed by a broad trapezoidal plateau between D_1 (~8.2 μm) and D_3 (~12.1 μm). Interestingly, $AUG_{S,0}$ looks similar to $AUG_{M,50}$ and $AUG_{L,40}$.

As regolith porosity increases, low spectral contrast features within the 10-μm region shallow, and a large minimum around 11.8 μm (D_3) deepens. In $AUG_{ML,0–90}$, D_3 begins to form a 'V' shape around 40% ($AUG_{M,40}$) and 70% ($AUG_{L,70}$) regolith porosity, whereas the 'V' shape is already clearly present in $AUG_{S,0}$. With increasing regolith porosity, the trapezoidal features in the 15-μm region decrease in spectral contrast until they disappear entirely in $AUG_{M,50}$ and $AUG_{L,60}$. The maximum at ~10.15 μm (P_3) is the most prominent maximum at high regolith porosities, and is the central feature of the 10-μm plateau.

3.6. Enstatite + Fayalite (MXT)

The 0% regolith porosity spectra of all three grain sizes in MXT ($MXT_{SML,0}$) look quite different from one another (Fig. 8). $MXT_{S,0}$ is the flattest spectrum of the three and has a series of shallow maxima and minima in the 10-μm region. $MXT_{M,0}$ contains a similar series of maxima and minima in the 10-μm region, but the features are deeper, and a minimum at ~18.47 μm (D_9) is present. $MXT_{L,0}$ has the same series of deep features, but is much deeper compared to $MXT_{M,0}$. It is possible maxima at ~8.48 μm (P_2) and 9.20 μm (P_3) are CFs that correspond to olivine and enstatite, which make up ~50% of the silicate sample.

As the regolith porosity increases, the individual features in the 10-μm region shallow. However, the spectral contrast of the 10-μm plateau in $MXT_{S,0–90}$ increases, similar to the trends we found for other pyroxenes. A shallower 10-μm plateau forms in $MXT_{M,0–90}$, but it is less trapezoidal compared to $MXT_{S,0–90}$, and the minimum that defines the long wavelength edge of the plateau (D_6) is much shallower compared to

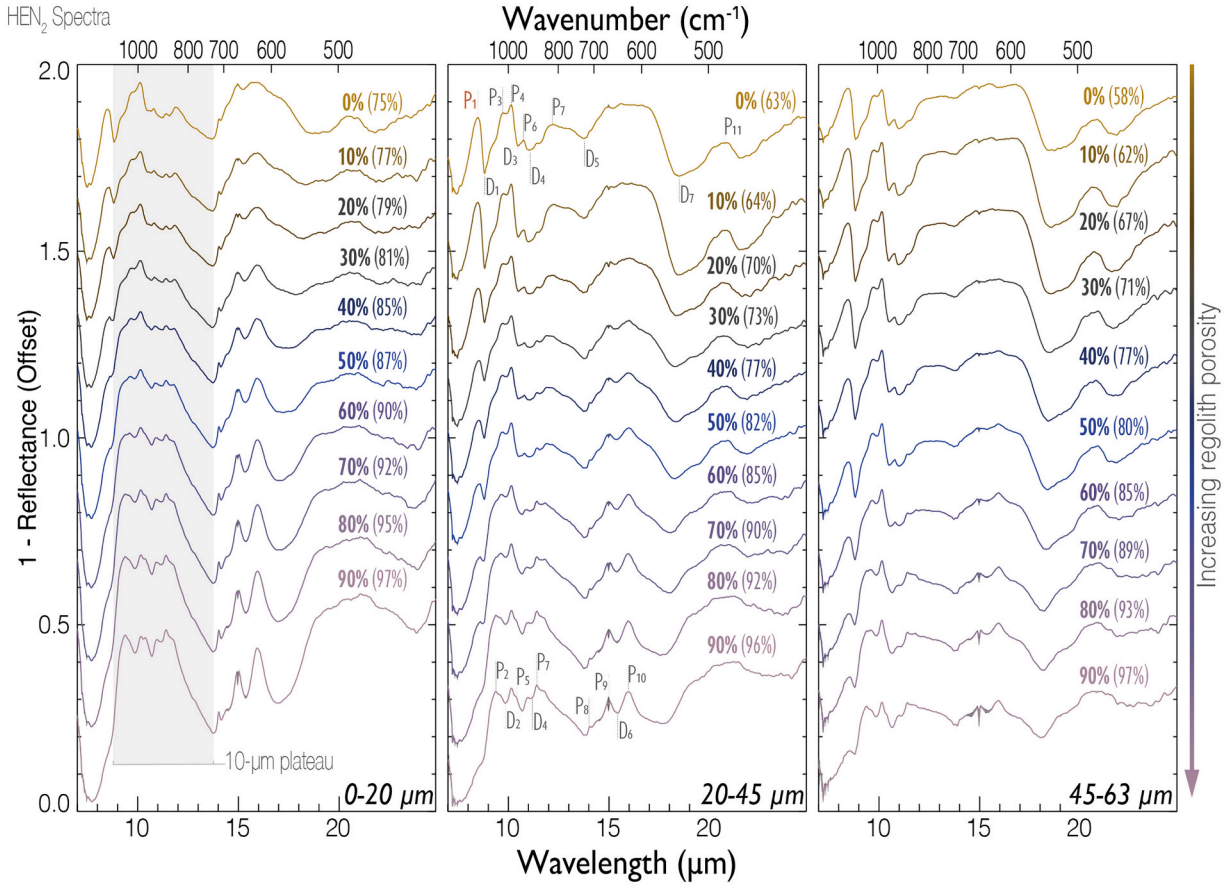

Fig. 5. Spectra of HEN_2 powder mixed with increasing wt% of KBr (from top to bottom) to represent regolith porosity. Gray region around the spectral curve represents standard deviation between each measurement of a given samples (i.e., sample heterogeneity). Bold percentages listed for each spectra represent the weight percent of KBr, while the percentages in parentheses are total simulated porosity (units of vol%). Each panel contains a different range of particle sizes (from left to right: 0–20, 20–45, and 45–63 μm). Spectra have been vertically offset for clarity and features are labeled in the 20–45 μm panel. The 20–45 μm spectral plot shows maxima labeled with 'P' and minima labeled with 'D'. The CF_1 (P_1) is labeled in red. The approximate 10-μm plateau region is shaded slightly in the 0–20 μm plot. (For interpretation of the references to colour in this figure legend, the reader is referred to the web version of this article.)

the other spectra described in this paper. $MXT_{L,0–90}$ does not form a 10-μm plateau. Rather, P_4 (~10.03 μm) and P_5 (~10.60 μm) remain, and a triangular maximum forms around 11.95 μm (P_8). The triangular maximum can also be seen in $MXT_{M,50–90}$, and it eventually becomes the long wavelength side of the 10 μm plateau.

3.7. 10-μm plateau trends

The 10-μm plateau is a feature that becomes more prominent in MIR spectra as regolith porosity increases. It is a silicate emission feature that is roughly trapezoidal and spans the 10-μm region, whose exact shape is dependent on mineralogy (Martin et al., 2022). The 10-μm plateau starts in one of two places; at a minimum around 7.5 μm found on the short-wavelength side of CF_1, or at the minimum of the steep minimum on the long wavelength side of CF_1, identified as D_1 in all spectra except ENS. We refer to these two boundary definitions as 'Lower' and 'Upper' respectively. The 10-μm plateau extends to the transparency feature region near the following minima; D_5 ($AEG_{SML,0–90}$, $HEN_{1,SML,0–90}$, $HEN_{2,SML0–90}$, $DIOP_{2,SML,0–90}$), D_8 ($DIOP_{1,SML,0–90}$), D_3 ($AUG_{SML,0–90}$), D_4 ($ENS_{SML,0–90}$). As was done in Martin et al. (2022), we calculated the width, spectral contrast, center location, skew, and slope of the 10-μm plateau.

We found the spectral contrast of the 10-μm plateau increases exponentially with increasing regolith porosity (Fig. 9). This result is consistent with results in Martin et al. (2022). The decrease in spectral contrast can be seen in all our spectral suites, regardless of mineralogy, or particle size fraction. Some spectral contrast trends contain a small bump centered on ~20% regolith porosity including $AEG_{SML,0–90}$, $AUG_{ML,0–90}$, $ENS_{,SML,0–90}$, and $DIOP_{2,SM,0–90}$. The other features we explored (band maximum, skew and slope) did not show any significant trends with regolith porosity. Data tables for these parameters, and the spectral contrast, can be found in the supplementary material.

4. Discussion

We have shown the MIR spectra of eight minerals and how they vary as a function of wt% KBr. With detailed spectral analysis, we outlined various feature parameters that change as a function of regolith porosity for the three particle sizes studied. Here, we discuss scattering regimes, as well as specific features that may be useful for remote sensing observations: the CFs, the spectral contrast of the 10-μm plateau, and the reststrahlen and fundamental vibrational bands of each sample.[1]

4.1. Scattering regimes

In our previous work (Martin et al., 2022), we showed that increasing the regolith porosity of our olivine samples resulted in spectra that contained features characteristic of both surface scattering

[1] A more detailed discussion can be found in PhD. dissertation, Martin, (2022).

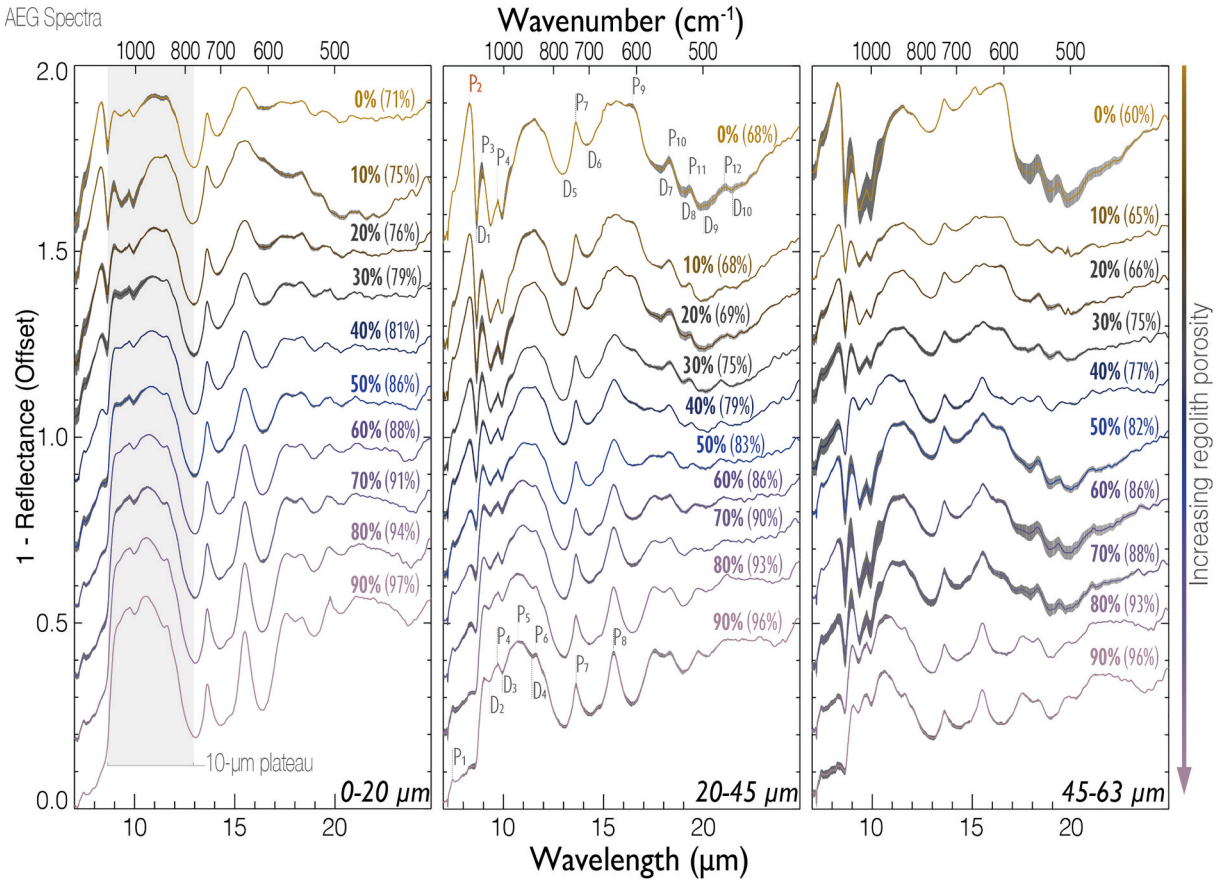

Fig. 6. Spectra of AEG powder mixed with increasing wt% of KBr (from top to bottom) to represent regolith porosity. Gray region around the spectral curve represents standard deviation between each measurement of a given samples (i.e., sample heterogeneity). Bold percentages listed for each spectra represent the weight percent of KBr, while the percentages in parentheses are total simulated porosity (units of vol%). Each panel contains a different range of particle sizes (from left to right: 0–20, 20–45, and 45–63 μm). Spectra have been vertically offset for clarity and features are labeled in the 20–45 μm panel. The 20–45 μm spectral plot shows maxima labeled with 'P' and minima labeled with 'D'. The CF_1 (P_2) is labeled in red. The approximate 10-μm plateau region is shaded slightly in the 0–20 μm plot. (For interpretation of the references to colour in this figure legend, the reader is referred to the web version of this article.)

(dominant at low regolith porosities) and volume scattering (dominant at high regolith porosities), leading us to conclude that the olivine samples gradually transitioned between surface and volume scattering regimes as the regolith porosity was increased. We also found that this transition depends on the particle size fraction of the sample, and that samples with smaller particle sizes more readily transition into volume scattering when regolith porosity is increased. All these trends are also observed in our pyroxene samples.

The transition from surface to volume scattering can be monitored using the CFs (both primary and secondary), as CFs are purely scattering features that are not caused by fundamental vibrations in the silicate mineral lattice. As such, CFs should only appear in a spectrum when surface scattering dominates, and they should decrease in spectral contrast as a surface scattering dominated spectrum transitions into a volume scattering dominated spectrum, which we observed as we increased the regolith porosity. For example, P_2 is the CF in $AEG_{SML,0–90}$ (Fig. 6). When $AEG_{S,0–90}$ has a regolith porosity of >50% the spectral contrast of the CF is zero and no feature can be identified. However, in $AEG_{L,0–90}$, the CF is identified even at 90% regolith porosity, though the spectral contrast has decreased by ~60% from $AEG_{L,0}$ to $AEG_{L,90}$. We predict that adding >90 wt% KBr into the sample mixture would result in the CFs continuing to decrease until they are completely below the noise level.

An additional line of evidence that the spectra of pyroxene transition from surface to volume scattering is the similarity of pyroxene spectra presented here and spectra known to be in the surface or volume scattering regimes. As we show in the following sections, reflectance spectra in the surface scattering regime from Hamilton (2000), Lane et al. (2011), and minerals from the Johns Hopkins University (JHU) spectral library are more similar to our low regolith porosity spectra, while spectra from Chihara et al. (2002), Koike et al. (1993, 2000, 2003), as well as emission spectra from the Berlin Emissivity Database (BED) are much better spectral analogs to our high porosity spectra.

4.2. 10-μm plateau

The spectral contrast of the entire 10-μm plateau (~8 to 13 μm – depending on the mineral composition) exponentially increases with increasing regolith porosity for nearly all pyroxene spectral suites (Fig. 9). $HEN_{2,L,0–90}$ and $DIOP_{2,L,0–90}$ show a much smaller increase in spectral contrast than the other spectral suites, but their spectral contrasts still follow the same general trend. In all spectral suites, the spectral contrast increase is much stronger for spectra of the smallest particle size fractions (i.e., $PYX_{a,S,0–90}$) than it is for spectra of medium and large particle size fractions (i.e., $PYX_{a,ML,0–90}$). For example, the $AEG_{S,90}$ 10-μm plateau spectral contrast is ~138%, compared to the $AEG_{M,90}$ spectral contrast of ~78%. At low regolith porosities (below ~40%), the spectral contrast average is below 20%.

Some 10-μm plateau trends also exhibit a small spectral contrast increase at low regolith porosities (≲30%), resulting in spectral contrast minimum at ~40–50% regolith porosity. The small increase at low porosities is quite pronounced in $ENS_{SML,0–90}$ spectra and to a lesser extent

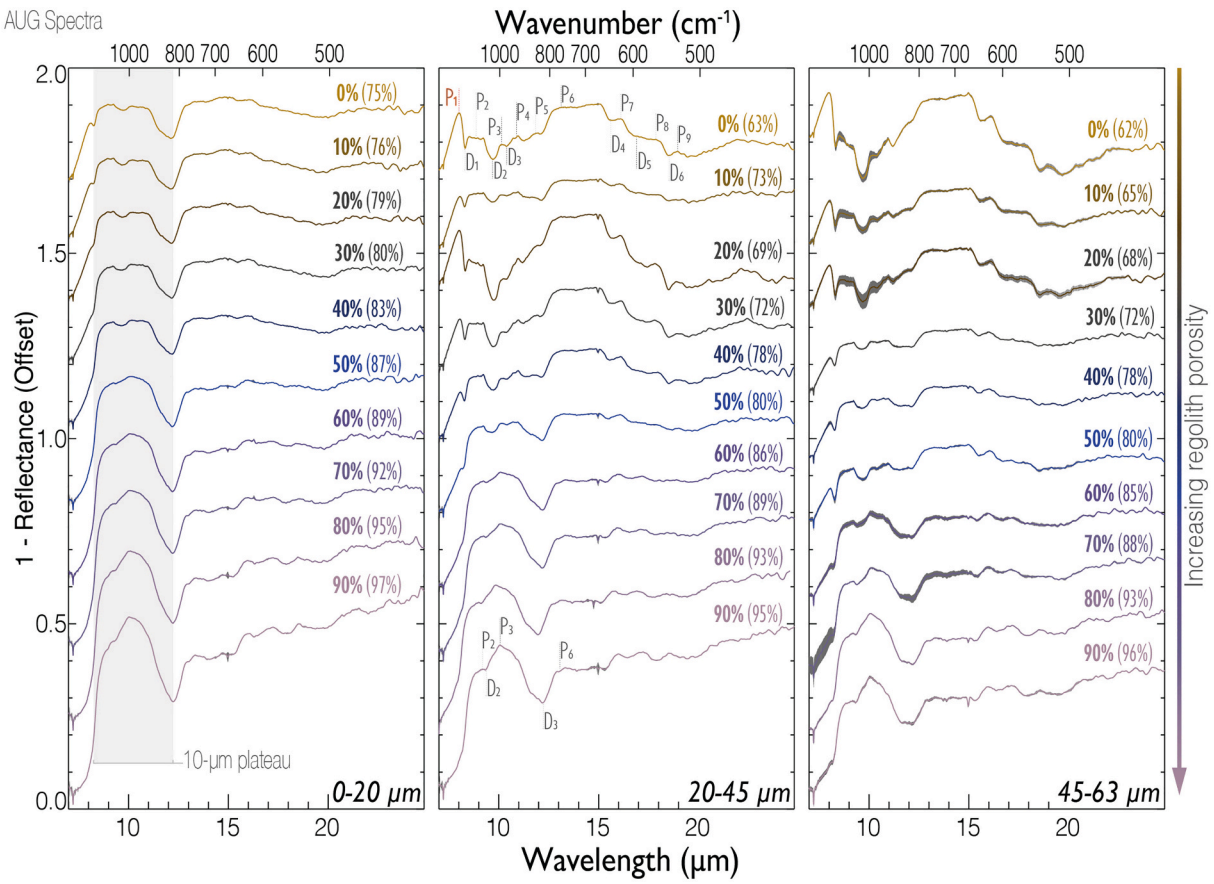

Fig. 7. Spectra of AUG powder mixed with increasing wt% of KBr (from top to bottom) to represent regolith porosity. Gray region around the spectral curve represents standard deviation between each measurement of a given samples (i.e., sample heterogeneity). Bold percentages listed for each spectra represent the weight percent of KBr, while the percentages in parentheses are total simulated porosity (units of vol%). Each panel contains a different range of particle sizes (from left to right: 0–20, 20–45, and 45–63 μm). Spectra have been vertically offset for clarity and features are labeled in the 20–45 μm panel. The 20–45 μm spectral plot shows maxima labeled with 'P' and minima labeled with 'D'. The CF_1 (P_1) is labeled in red. The approximate 10-μm plateau region is shaded slightly in the 0–20 μm plot. (For interpretation of the references to colour in this figure legend, the reader is referred to the web version of this article.)

in $AUG_{M,0–90}$. Rather than being a physical phenomenon, we attribute this trend to how we have defined the 10-μm plateau. At these low regolith porosities, some spectra, such as $ENS_{SML,0}$, do not exhibit a 10-μm plateau at all. In these cases, the spectral contrast values are more representative of the contrast between the TF and the largest maximum in the 10-μm region rather than the actual contrast of the 10-μm plateau.

4.3. Enstatite

4.3.1. Surface scattering dominated spectra

By comparing $ENS_{SML,0–90}$ to spectra of compositionally similar enstatite (Mg_{91}; Hamilton, 2000) in the surface scattering regime, we assign as D_2, D_3, D_6, D_7, and D_8 as RBs (Table 4). In addition to these features, the general shape of their enstatite spectrum matches $ENS_{SML,0}$. The following spectral characteristics are present in both the enstatite spectra presented here, and in the Hamilton (2000) enstatite spectra: a shallow minimum between P_5 and P_6, and between P_7 and P_8, the trapezoidal shape of P_9, and a broad rise from the P_{10} region to ~16 μm with a minimum and maxima the correspond to D_5, P_{15}, and P_{16}.

As D_2, D_3 D_7, and D_8 are likely RBs, they can be used as indicators of pyroxene composition in surface scattering dominated spectra. The spectral contrasts of D_2 and D_3 linearly decrease with increasing regolith porosity, and we thus estimate they are useful for mineral identification until ~30% regolith porosity (Fig. 1). In $ENS_{S,0–90}$, D_3 has a much smaller spectral contrast at low regolith porosities, while the spectral contrast of D_2 is not as dependent on particle size. The RB, D_6, is not listed as a useful indicator because it shifts ~1 μm to shorter wavelengths with increasing regolith porosity. Though not on its own, the relative position of D_6 to D_7 and D_8 can be useful for mineralogical identification.

4.3.2. Volume scattering dominated spectra

In high porosity spectra dominated by volume scattering, we tentatively identify P_4, P_{10}, P_{14}, P_{15}, and P_{17} as vibrational stretching bands, which is consistent with band shape and position measurements reported in Chihara et al. (2002), where spectra were measured in the volume scattering regime (Table 4). Although Chihara et al. (2002) do not provide band numbers, we will refer to the maxima in their spectra numerically beginning at the shortest wavelength as 'C_x'. Though P_4 is present in low regolith porosity spectra, we interpret it as a vibrational stretching band in the volume scattering regime, even in 0% regolith porosity spectra (i.e., $ENS_{SML,0}$). As P_4 is in a broad minimum between P_1 and P_5, we argue that P_4 is the inverted RB located at ~9.17 μm. P_{10} shifts 0.23 (0–20 μm), 0.52 (20–45 μm), and 0.51 μm (45–63 μm) shortward as regolith porosity increases. $ENS_{SML,0}$, and in the Hamilton (2000) spectrum, enstatite spectra exhibit a broad and tilted shoulder (or flection) in the general region of P_{10}, possibly due to being located between an RB and a transparency region. As volume scattering begins to dominate, C_6 (11.6 μm), a fundamental band identified in Chihara et al. (2002), increases in strength relative to the surrounding features. A complex dependency between closely-neighboring features that transition into the volume scattering regime at different regolith porosities could explain the migration of P_{10} to ~11.6 μm. For example, D_4 increases in spectral contrast with increasing regolith porosity, possibly

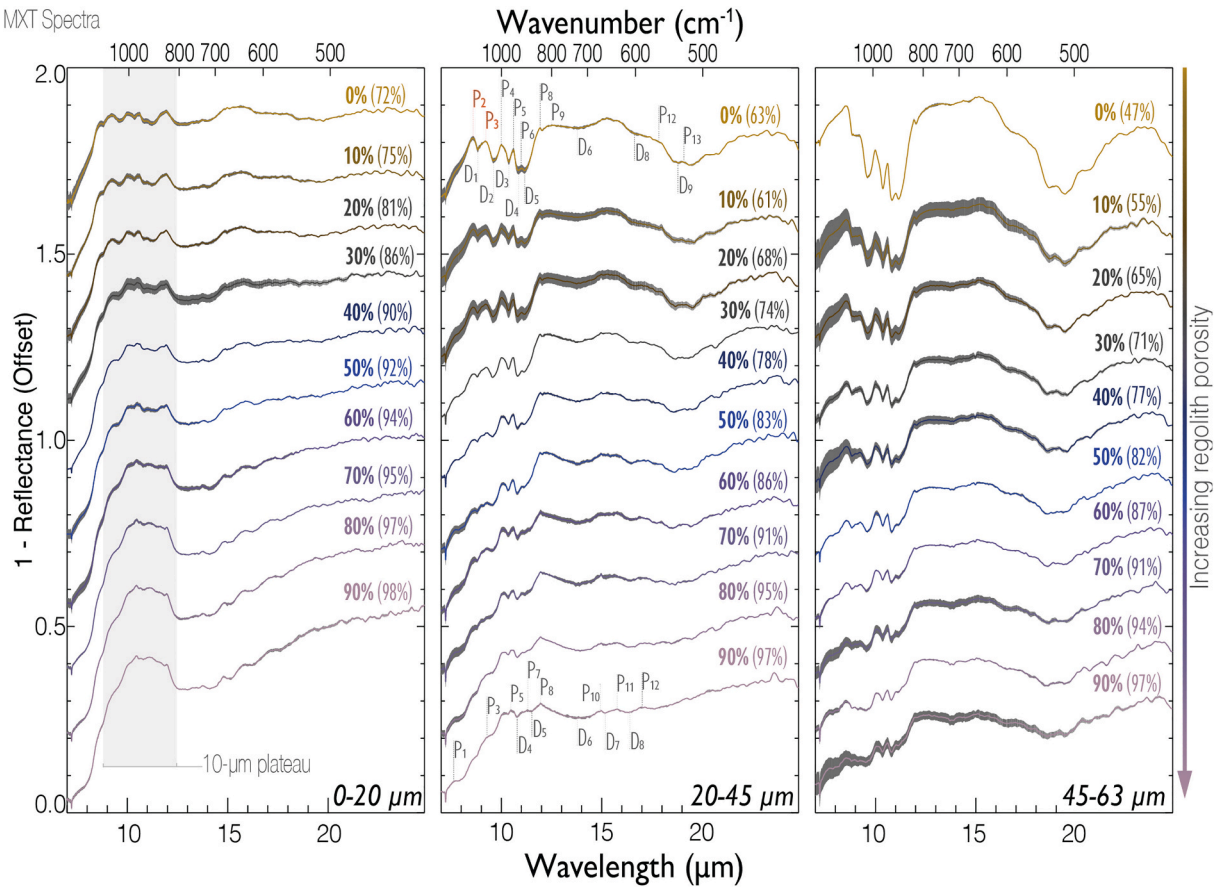

Fig. 8. Spectra of MXT powder mixed with increasing wt% of KBr (from top to bottom) to represent regolith porosity. Gray region around the spectral curve represents standard deviation between each measurement of a given samples (i.e., sample heterogeneity). Bold percentages listed for each spectra represent the weight percent of KBr, while the percentages in parentheses are total simulated porosity (units of vol%). Each panel contains a different range of particle sizes (from left to right: 0–20, 20–45, and 45–63 μm). Spectra have been vertically offset for clarity and features are labeled in the 20–45 μm panel. The 20–45 μm spectral plot shows maxima labeled with 'P' and minima labeled with 'D'. The two possible CF_1 (P_2 and P_3) are labeled in red. The approximate 10-μm plateau region is shaded slightly in the 0–20 μm plot. (For interpretation of the references to colour in this figure legend, the reader is referred to the web version of this article.)

transitioning to the volume scattering regime at a slower rate compared to P_{10}. As such, the position of P_{10} could be 'pulled' to longer wavelengths while D_4 is still in the surface scattering regime.

In the volume scattering-dominant regime, the positions of P_4, P_{10}, P_{14}, and P_{15} can be used for compositional identification, while the presence of features with the same shape and general position as the triplet P_{11}, P_{12}, and P_{13} (a 'triplet' feature) is a good indicator of enstatite. Since P_{10} migrates an average of 0.42 μm to shorter wavelengths, this maximum alone is not recommended for mineral/compositional characterization if the scattering regime is not known. Rather, P_4, a likely vibrational band that does not migrate with increased regolith porosity, is better for compositional analysis with a spectrum of unknown scattering regime. At longer wavelengths, the maxima within the 'triplet' are not identified as vibrational bands, while P_{14} and P_{15} are. Maxima that are roughly equivalent those in the triplet are seen in enstatite spectra in Chihara et al. (2002; Fig. 1), but the exact location of the equivalent Chihara et al. maxima are not the same as the triplet maxima. As such, the presence of features that make up the triplet are good indicators of the mineral enstatite, but not for determining the enstatite Mg#.

4.4. Diopsides

4.4.1. Surface scattering dominated spectra

In samples of low regolith porosity, we can compare our spectra to emissivity spectra of diopsides NMNH-80819 (Mg_{90}) and BUR-1820 (Mg_{92}), reported in Hamilton (2000), and assign RBs to $DIOP_{1,SML,0}$ and $DIOP_{2,SML,0}$ respectively (Table 5). We refer to critical absorptions as 'H_x', with 'x' referring to the number identified in Hamilton (2000). Many of the NMNH-80819 absorptions align well with $DIOP_{1,SML,0}$, though some longer wavelength bands do not. Hamilton (2000) identifies an RB around 20.7 μm that may correspond to D_{11} (~19.7 μm) in $DIOP_{1,SML,0}$, though it is at a slightly shorter wavelength. The position of a band is more sensitive to composition at longer wavelengths (e.g., Chihara et al., 2002; Koike et al., 2003), so the difference in composition may result in feature positions that are increasingly different compared to the positions of corresponding RBs in Hamilton (2000).

BUR-1820 is the closest compositional analog to $DIOP_2$, but there are a few differences. Minima in 0% regolith spectra (i.e., $DIOP_{2,SML,0}$) may be offset compared to BUR-1820 due to possible contamination from additional high Mg-pyroxene phases that were not entirely removed from the $DIOP_2$ sample, such as Mg_{96} enstatite. In particular, D_7 (~17.6 μm) and D_8 (~19.7 μm) look very similar to H_4 (~18.0 μm) and H_5 (~20.8 μm), but are at slightly shorter wavelengths. Due to uncertainty from different wavelength positions, we refrain from giving D_7 and D_8 RB designations. Thus, at low regolith porosities we assign D_4, D_5, D_{10}, and D_{11}, as $DIOP_{1,SML,0}$ RBs, and D_2 and D_3 as $DIOP_{2,SML,0}$ RBs.

At low regolith porosities the positions of RBs $D_{4/5}$ in $DIOP_{1,SML,0}$ and $D_{2/3}$ in $DIOP_{2,SML,0}$ are good indicators of composition, as their positions do not shift substantially with regolith porosity changes (Figs. 2 and 3). Though D_{10} and D_{11} are likely RBs in $DIOP_{2,SML,0}$ as well, their positions shift to shorter wavelengths with increasing regolith porosity, and thus

Table 3
Features with spectral contrasts that positively (↗) and negatively (↘) trend with increasing regolith porosity. Features that trend in the opposite direction in one particle size compared to the other two are underlined and indicated in italic.

Sample		Feature		
		0–20 μm	20–45 μm	45–63 μm
ENS	↗	P_4, P_{10}, P_{11}, P_{12}, P_{13}, P_{14}, P_{15}, D_6	P_4, P_{10}, P_{11}, P_{12}, P_{13}, P_{14}, P_{15}, D_4, D_6	*P_3*, P_4, P_{10}, P_{11}, P_{12}, P_{13}, P_{14}, P_{15}, D_4, D_6
	↘	P_1, P_2, P_3, P_5, P_6, D_1, D_2, D_3, *D_4*, D_5, D_7, D_8	P_1, P_2, P_3, P_5, P_6, P_7, P_9, P_{17}, P_{18}, P_{19}, D_1, D_2, D_3, D_5, D_7, D_8	P_1, P_2, P_5, P_6, P_7, *P_8*, P_9, *P_{16}*, P_{17}, P_{18}, P_{19}, D_1, D_2, D_3, D_5, D_7, D_8
$DIOP_1$	↗	P_2, P_4, *P_5*, P_8, P_9, P_{10}, P_{11}, D_2, *D_9*	P_2, P_4, P_6, P_8, P_9, P_{10}, P_{11}, D_2	P_2, P_4, P_6, *P_7*, P_8, P_9, P_{10}, D_2
	↘	P_1, P_3, P_7, P_{12}, D_1, D_3, D_4, D_5, D_7, D_8, D_{10}, D_{11}	P_1, P_3, P_5, P_7, P_{12}, D_1, D_3, D_4, D_5, *D_6*, D_7, D_8, D_9, D_{10}, D_{11}	P_1, P_3, P_5, *P_{11}*, P_{12}, D_1, D_3, D_4, D_5, D_8, D_9, D_{10}, D_{11}
$DIOP_2$	↗	P_2, P_3, *P_5*, P_6, P_7, P_8, P_9, *P_{10}*, D_5, *D_6*	P_2, P_3, P_6, P_8, P_9	P_2, P_3, P_6, P_8, *P_{11}*, D_5
	↘	P_1, P_4, D_1, D_2, D_3, D_8	P_1, P_4, *P_7*, P_{10}, D_1, D_2, D_3, *D_5*, D_7, D_8	P_1, P_4, *P_5*, *P_9*, P_{10}, D_1, D_2, D_3, *D_6*, D_7, D_8
HEN_1	↗	P_2, P_3, P_5, P_6, P_8, P_9, P_{10}, *D_3*, D_6, *D_7*	P_2, P_3, P_5, P_6, P_7, P_8, P_9, P_{10}, *D_2*, D_6	P_2, P_3, P_6, P_7, P_8, P_9, D_6
	↘	P_1, P_4, D_1, D_2, D_4, D_5	P_1, P_4, D_1, D_4, D_5, D_7	P_1, D_1, D_4, D_5, D_7
HEN_2	↗	P_2, P_3, *P_5*, *P_6*, P_8, P_9, P_{10}, P_{11}, *D_3*	P_2, P_3, P_8, P_9, P_{10}, P_{11}	P_2, P_3, *P_4*, *P_7*, P_9, P_{10}, P_{11}
	↘	P_1, P_4, D_1, D_2, D_4, D_5, D_6, D_7	P_1, P_4, P_6, D_1, D_2, D_3, D_4, D_5, D_6, D_7	P_1, P_6, D_1, D_2, D_3, D_4, D_5, D_6, D_7
AEG	↗	P_1, P_4, P_5, P_6, P_7, P_8, P_{10}, P_{12}, P_{13}, D_7, D_9, D_{10}	P_1, *P_3*, P_4, P_5, P_6, P_7, P_8, P_{10}, P_{12}, P_{13}, D_4, D_7, D_9	P_1, P_4, P_5, P_6, P_7, P_8, P_{10}, P_{12}, D_4
	↘	P_2, *P_3*, D_1, D_2, D_3, *D_4*, D_5, D_6	P_2, D_1, D_2, D_3, D_5, D_6, D_8, *D_{10}*	P_2, *P_9*, D_1, D_2, D_5, D_6, *D_7*, D_8, *D_9*
AUG	↗	P_3, P_6, P_7, *P_8*, *P_9*, D_6	P_3, P_6, P_7, D_3, D_6	P_3, P_6, P_7, D_3, D_6
	↘	P_1, D_2, *D_3*, D_4, *D_5*	P_1, P_2, P_5, P_8, D_1, D_2, D_4, D_6	P_1, P_2, *P_4*, P_5, P_8, D_1, D_2, D_4, D_6
MXT	↗	*P_6*, P_7, P_{10}, *P_{12}*, P_{13}	P_1, P_7, *P_8*, P_{10}, *P_{11}*, P_{13}, *D_7*	P_1, *P_9*, P_{13}, *D_8*
	↘	*P_1*, P_4, P_8, *P_{11}*, D_1, D_2, D_3, D_4, D_5, D_6, *D_7*, D_8, D_9	P_2, P_3, P_4, P_5, P_6, *P_9*, P_{12}, D_1, D_2, D_3, D_4, D_5, D_6, D_8, D_9	P_2, P_3, P_4, P_5, P_6, *P_8*, P_{12}, *P_{13}*, D_1, D_2, D_3, D_4, D_5, D_9

are not as reliable as $D_{4/5}$ in $DIOP_{1,SML,0}$ spectra.

4.4.2. *Volume scattering dominated spectra*

At high regolith porosities, many spectral peaks are similar to peaks observed in absorption spectra of diopside (Koike et al., 2000; Table 5). Although Koike et al. (2000) do not provide band numbers, we will refer to the maxima in their spectra numerically beginning at the shortest wavelength as 'K_x'. Additionally, we note that the Koike et al. (2000) diopside was grown synthetically and is therefore the pure Mg-rich endmember (contains no amount of Fe), unlike $DIOP_1$ and $DIOP_2$. As such, there are slight position differences, likely due to the aforementioned compositional differences. In terms of general shape, $DIOP_{1,SML,90}$ and $DIOP_{2,SML,90}$ do not exhibit the expected three-pronged 10-μm region feature that is seen in diopside and hedenbergite spectra (e.g., $HEN_{1,SML,90}$ and $HEN_{2,SML,90}$; see Section 4.5). Rather, the outer prongs are much smaller compared to K_1 and K_4, while the middle prong is much more pronounced compared to K_2. This difference in shape may be due to each band transitioning into the volume scattering regime at different porosities, with P_4 transitioning first. Additionally, apparent simultaneous growth of P_3 and decrease of P_4 with increasing regolith

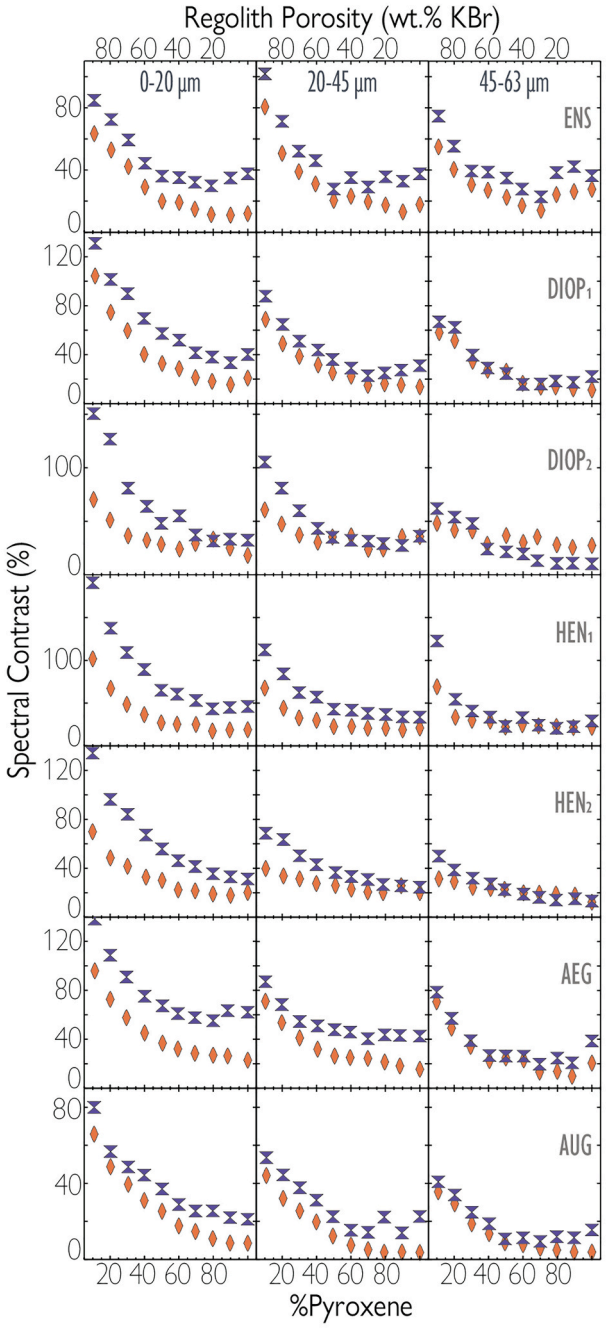

Fig. 9. Spectral contrast of the 10-μm plateau for in each pyroxene as a function of regolith porosity. Each column is a different particle size bin: 0–20 μm (left), 20–45 μm (middle), and 45–63 μm (right). The Upper, and Lower continua are denoted with orange diamonds, and purple hourglasses respectively. The upper x-axis shows the corresponding regolith porosity. (For interpretation of the references to colour in this figure legend, the reader is referred to the web version of this article.)

porosity suggests a slightly more complicated relationship between the bands due to the incorporation of Fe in the $DIOP_1$ and $DIOP_2$ samples. P_7 (~12.48 μm) in $DIOP_{2,SML,90}$ does not correspond to any maxima in the Koike et al. (2000) diopside spectra, and may be due to the small amount of Mg_{96} enstatite (Table 1) present in the samples. Chihara et al. (2002) report a Mg_{90} enstatite with a small maximum at 12.5 μm, which corresponds to the P_7 position. As there are no fundamental diopside vibrational modes here, the small fraction of enstatite is enough to produce this small maximum. Diopside bands are much stronger than

Table 4
Average minima positions that correspond to RBs identified in Hamilton (2000) (H_x), and maxima that correspond to bands in Chihara et al. (2002) (C_x). Bands useful for compositional identification or regolith porosity estimation are underlined.

ENS feature	Ave. position (μm)	Cor. band	Cor. band position (μm)
$\underline{D_2}$	10.21 μm	H_2	10.20 μm
$\underline{D_3}$	11.47 μm	H_4	11.50 μm
D_6	17.38 μm	H_5	17.54 μm
$\underline{D_7}$	18.28 μm	H_6	18.25 μm
$\underline{D_8}$	19.46 μm	H_7	19.57 μm
$\underline{P_4}$	9.29 μm	H_1/C_2	9.17 μm
$\underline{P_{10}}$	11.57 μm	C_6	11.6 μm
$\underline{P_{14}}$	14.53 μm	C_{11}	14.7 μm
$\underline{P_{15}}$	15.45 μm	C_{12}	15.5 μm
P_{17}	17.89 μm	C_{13}	17.7 μm

the enstatite at other wavelengths, and thus mask additional enstatite features.

P_4, P_9, and P_{10} in $DIOP_{1,SML,0–90}$ and P_3, P_8, and P_9 in $DIOP_{2,SML,0–90}$ all likely correspond to resonance bands, and do not shift considerably with increasing regolith porosity. As such, they are all useful features for mineral identification. A small caveat in using $P_{9/10}$ and $P_{8/9}$ in $DIOP_{1,L,0–90}$ and $DIOP_{2,L,0–90}$ respectively, is that these features tend to only appear as two distinct maxima when regolith porosity is high, and particle size fractions are low. So, we recommend only these double features when their individual positions can be spectrally distinguished.

4.5. Hedenbergites

4.5.1. Surface scattering dominated spectra

The two hedenbergites (HEN_1 and HEN_2) are similar in composition to Hamilton (2000) samples NMNH-R11524 (Mg_7) and HS-10.4B (Mg_{26}), and we assign D_3, D_4, and potentially D_7 as RBs in both HEN_1 and HEN_2 (Table 6). Slight differences in EMP analysis show HEN_1 with 6.75 wt% MnO, 0.83 wt% MgO, and 20.58 wt% FeO, whereas NMNH-R11524 has 3.27 wt% MnO, 1.06 wt% MgO, and 22.63 wt% FeO, which may explain slight differences in position between RBs and $HEN_{1,SML,0–90}$ minima. Additionally, the HEN_2 Mg# is roughly half that of HS-10.4B, so the differences in minima positions are expected (Table 6). In addition to the minima Hamilton (2000) identifies, the general shape of their clinopyroxene spectra matches $HEN_{1,SML,0}$ and $HEN_{2,SML,0}$. For example, $HEN_{1,SML,0}$, $HEN_{2,SML,0}$, NMNH-R11524, and HS-10.4B all show a shallow minimum between P_3 and P_4 and the trapezoidal shape between D_5 and D_7.

There is one minimum, D_5 (~13.7 μm), in low porosity spectra of both HEN_1 and HEN_2 (Figs. 4 and 5) that does not correspond to the clinopyroxene emissivity spectra reported in Hamilton (2000). Though both hedenbergite samples are natural, they are unlikely to contain extraneous mineral phases based on the EMP analysis so D_5 is likely not an RB. Rather, we argue the spectral region around D_5 is transitioning into volume scattering more readily than the spectral regions at longer and shorter wavelengths, causing the minimum. As samples increase in regolith porosity, D_5 increases in spectral contrast, and is eventually identifiable as a region of low spectral absorbance when regolith porosity is high.

When surface scattering is dominant (i.e., low regolith porosity) D_3 and D_4 in both $HEN_{1,SML,0–90}$ and $HEN_{2,SML,0–90}$ do not shift position substantially with changing porosity (Figs. 4 and 5; see supplemental material for value of exact position), are RBs, and thus are potential indicators of composition regardless of regolith porosity. The spectral contrast of P_6, the maximum between D_3 and D_4, is rather small at low regolith porosities (≲40% regolith porosity), which makes it potentially difficult to distinguish individual minima for remote sensing applications.

4.5.2. Volume scattering dominated spectra

In volume scattering dominant spectra, the following maxima correspond to fundamental vibrational bands in high porosity spectra: P_2, P_5, P_6, P_7, P_8, P_9, for $HEN_{1,SML,90}$, and P_2, P_5, P_6, P_7, P_9, P_{10}, for $HEN_{2,SML,90}$ (Table 6). As there are few, if any, hedenbergite absorption

Table 5
Average position of minima that correspond to RBs identified in Hamilton (2000), and maxima that correspond to fundamental vibrational bands in Koike et al. (2000). Bands useful for compositional identification or regolith porosity estimation are underlined. *Indicates a tentative correspondence.

$DIOP_1$ feature	Ave. position (μm)	Cor. band	Cor. band position (μm)	$DIOP_2$ feature	Ave. position (μm)	Cor. band	Cor. band position (μm)
$\underline{D_4}$	10.56 μm	H_2	10.41 μm	$\underline{D_2}$	10.52 μm	H_2	10.4 μm
$\underline{D_5}$	11.09 μm	H_3	10.9 μm	$\underline{D_3}$	10.99 μm	H_3	10.9 μm
D_{10}	17.55 μm	H_4	17.8 μm				
$*D_{11}$	19.67 μm	H_5	20.7 μm				
P_2	9.33 μm	K_1	9.28 μm	P_2	9.28 μm	K_1	9.28 μm
$\underline{P_4}$	10.11 μm	K_2	10.29 μm	$\underline{P_3}$	10.05 μm	K_2	10.29 μm
P_5	10.80 μm	K_3	10.86 μm	P_5	10.83 μm	K_3	10.86 μm
P_6	11.45 μm	K_4	11.43 μm	P_6	11.47 μm	K_4	11.43 μm
$\underline{P_9}$	14.87 μm	K_6	14.82 μm	$\underline{P_8}$	14.91 μm	K_6	14.82 μm
$\underline{P_{10}}$	15.76 μm	K_7	15.76 μm	$\underline{P_9}$	15.72 μm	K_7	15.76 μm
P_{11}	19.43 μm	K_8	19.49 μm	P_{10}	19.55 μm	K_8	19.49 μm
P_{12}	20.54 μm	K_9	20.60 μm	P_{11}	20.82 μm	K_9	20.60 μm

Table 6
Average position of minima that correspond to RBs identified in Hamilton (2000) (H_x), and maxima that correspond to fundamental vibrational bands in Koike et al. (2000) (K_x). Bands useful for compositional identification or regolith porosity estimation are underlined. *Indicates a tentative correspondence.

HEN_1 feature	Ave. position (μm)	Cor. band	Cor. band position (μm)	HEN_2 feature	Cor. band	Ave. position (μm)	Cor. band position (μm)
$\underline{D_3}$	10.61 μm	H_2	10.49 μm	$\underline{D_3}$	H_2	10.53 μm	10.31 μm
$\underline{D_4}$	11.09 μm	H_3	11.29 μm	$\underline{D_4}$	H_3	11.09 μm	10.67 μm
$*D_7$	18.26 μm	H_4	19.34 μm	$*D_7$	H_4	18.62 μm	18.80 μm
P_2	9.36 μm	K_1	9.28 μm	P_2	K_1	9.38 μm	9.28 μm
$\underline{P_5}$	10.38 μm	K_2	10.29 μm	$\underline{P_5}$	K_2	10.32 μm	10.29 μm
P_6	10.97 μm	K_3	10.86 μm	P_6	K_3	10.99 μm	10.86 μm
P_7	11.48 μm	K_4	11.43 μm	P_7	K_4	11.49 μm	11.43 μm
$\underline{P_8}$	14.98 μm	K_6	14.82 μm	$\underline{P_9}$	K_6	14.98 μm	14.82 μm
$\underline{P_9}$	15.93 μm	K_7	15.76 μm	$\underline{P_{10}}$	K_7	15.94 μm	15.76 μm
$*P_{10}$	21.24 μm	K_9	20.60 μm	$*P_{11}$	K_9	21.09 μm	20.60 μm

spectra in the literature, we compare our high porosity spectra of hedenbergites to diopside spectra from Koike et al. (2000). There are many similarities between maximum shapes of hedenbergite and diopside spectra, though diopside is a Mg-rich clinopyroxene, and hedenbergite is Fe-rich clinopyroxene. Despite their compositional differences, the overall shape of our hedenbergite spectra is very similar to the Koike diopside spectra. For example, $HEN_{1,SML,70–90}$ and $HEN_{2,S,80–90}$ exhibit a three-pronged 10-μm region feature that is clearly seen in the diopside spectrum (Koike et al., 2000; Fig. 1). The differences in feature positions are likely because HEN_1 and HEN_2 are hedenbergites (Fe-rich) and the Koike sample is diopside (Mg-rich). As both of these hedenbergites contained little to no potential other phases, we are confident the maxima listed in Table 6 correspond to fundamental vibrational bands in high porosity spectra – though P_{10} in $HEN_{1,SML,90}$, and P_{11} in $HEN_{2,SML,90}$ are "tentative" assignments due to the larger difference between their positions and the position of K_9.

There are a number of useful compositional hedenbergite markers in volume scattering dominant spectra: the general position of P_2, P_5, the double maxima $P_{8/9}$ ($HEN_{1,SML,90}$) and $P_{9/10}$ ($HEN_{2,SML,90}$), and the three-pronged shape of 10-μm plateau. At regolith porosities below ~50% (depending on particle size fractions) P_6 and P_7 are two distinct maxima separated by a broad D_4 (Figs. 4 and 5). As regolith porosity increases, D_4 narrows and P_7 shifts closer to P_6. At high regolith porosities (≳60%), D_4 is very shallow, making P_6 and P_7 appear as a singular feature with a small D_4 divot at the apex. A more reliable maximum is P_4, which we identify at each regolith porosity step. At high regolith porosities P_4 is joined by P_5 to make a double-peaked maximum. The composite of the double-maximum can be used for mineralogical and/or compositional characterization at high regolith porosities, if P_4 and P_5 are unresolvable. In $HEN_{1,S,0–90}$ and $HEN_{2,SM,0–90}$ P_2 does not shift, unlike in $HEN_{1,ML,0–90}$ and $HEN_{2,L,0–90}$. As such, the general position of P_2 may be a good indicator of mineralogy, but the exact position should not be used for compositional analysis unless the scattering regime is known to be volume scattering. For an astronomical surface with known hedenbergite, P_5 is the best indicator of composition if the regolith porosity is sufficiently high (≳30%) and particle size is below ~45 μm, as this feature only appears under these conditions. Finally, as long as $P_{8/9}$ and $P_{9/10}$ are well-separated in a spectrum, they can be used for mineral and compositional characterization.

4.6. Aegirine

4.6.1. Surface scattering dominated spectra

In spectra of low regolith porosity AEG, we identify D_2 as an RB (Table 7). Though AEG is a remarkably pure aegirine (sometimes called acmite) sample, aegirine is a non-quadrilateral pyroxene, so it is relatively rare and has not been studied in as much detail as ortho- and clinopyroxenes. Hamilton (2000) presents a spectrum of acmite (LACMNH-6800) and describes the locations of RBs, but does not report the positions of the RBs. They discuss primary and secondary CFs, which are found near 8.4 μm and 16.7 μm, respectively, and correspond well to $AEG_{SML,0}$ P_2 (~8.33 μm) and P_9 (~16.39 μm). We previously identified these two maxima as the CFs based on their strong decrease in spectral contrast with increasing porosity. In addition to LACMNH-6800, we compared $AEG_{SML,0}$ to a coarse ground acmite spectrum (75–250 μm; sample NMNH-133746) in the Johns Hopkins University (JHU) spectral library. Many minima are similar in shape, and have roughly similar positions, but only one, D_2, is mentioned in literature. Hamilton (2000) describe nonquadrilateral spectra as having a singular broad feature in the 10-μm region (presumably corresponding to an RB). Fig. 3 in Hamilton (2000) corroborate this description and show superimposed fine-scale wiggles on the broad 10-μm region feature. As multiple RBs are not mentioned in Hamilton (2000), or any other literature, we only identify D_2 as an RB.

At low regolith porosities, D_2 can be used as a compositional indicator - so long as it can be identified. D_2 is not always present in the spectra, as its spectral contrast is highly dependent on particle size – the spectral contrast of D_2 in medium and large particle size fraction spectra (i.e., $AEG_{ML,0}$) is much higher than in the smallest particle size fraction spectrum (i.e., $AEG_{S,0}$). Furthermore, D_2 disappears in $AEG_{S,0–90}$ around 50% regolith porosity. This behavior is consistent with the identification of D_2 as an RB, as spectra of smaller particle sizes will more readily transition from surface to volume scattering as regolith porosity increases.

4.6.2. Volume scattering dominated spectra

We can compare $AEG_{SML,90}$ to absorption spectra of augite spectrum (Koike et al., 1993) and tentatively assign the following maxima as vibrational bands: P_4, P_5, P_6, P_7, P_8, P_{10}, and P_{11} (Table 7). We are not aware of any published aegirine absorption spectra, but augite can provide a reasonable comparison because AEG falls along the aegirine-augite solid solution. The maxima we identify in $AEG_{SML,90}$ are not in the same positions as Koike et al. augite maxima, but they look similar in terms of relative positions and spectral contrasts.

As P_4, P_6, P_7, P_8, P_{10}, and P_{11} are likely vibrational bands, and their positions remain stable regardless of regolith porosity (see Fig. 6; and supplemental material for exact positions), they are useful indicators of mineralogy and composition when looking at spectra in the volume scattering regime. Additionally, P_5 may be a good indicator of regolith porosity, through its position shifts to shorter wavelengths with increasing regolith porosity: 0.59 (0–20 μm), 0.68 (20–45 μm) and 0.89 μm (45–63 μm). Interestingly, P_5 bears a strong resemblance to the P_7 olivine maximum in Martin et al. (2022), which is a vibrational band indicative of regolith porosity. Though P_5 is likely a vibrational band, its exact position shifts with increasing regolith porosity, so it is not a useful maximum for mineral identification. However, like P_7 in olivine spectra, P_5 may be useful for estimations of regolith porosity.

4.7. Augite

As AUG is clearly a mixture of minerals, confidently identifying RBs is challenging, but we conclude that $AUG_{SML,0}$ likely contains jadeite, phlogopite, and hypersthene/enstatite features (Table 8). Based on Wo-En-Fs values from EMP analysis, AUG is an augite (a solid solution

Table 7
Average minima position that corresponds to minima from spectra in the JHU (J_x) spectral library that are likely RBs, and maxima that tentatively correspond to bands in Koike et al., 1993 (K_x). Bands useful for compositional identification or regolith porosity estimation are underlined.

AEG feature	Ave. position (μm)	Cor. band	Cor. band position (μm)
$\underline{D_2}$	9.35 μm	J_2	9.40 μm
$\underline{P_4}$	9.70 μm	K_1	9.29 μm
$\underline{P_5}$	10.61 μm	K_2	10.25 μm
$\underline{P_6}$	11.65 μm	K_3	11.35 μm
P_7	13.61 μm	K_4	14.82 μm
$\underline{P_8}$	15.50 μm	K_5	15.69 μm
$\underline{P_{10}}$	17.50 μm	K_6	19.29 μm
$\underline{P_{11}}$	18.32 μm	K_7	19.29 μm

Table 8
Average minima positions that may correspond to RBs identified from JHU and BED spectral libraries. The jadeite spectrum originates from Smithsonian sample NMNHB18463, and the hypersthene spectra originate from Smithsonian sample NMNHC2368 and BED spectrum comes from sample hypersthene_180c25_63.

AUG feature	Average position (μm)	Corresponding band position (μm)	Mineral
D_1	8.55 μm	8.55 μm	Jadeite
D_2	9.72 μm	9.43 μm	Hypersthene
D_3	11.23 μm	11.45 μm	Hypersthene
D_5	17.94 μm	17.63 μm	Hypersthene
D_6	18.54 μm	18.42 μm	Hypersthene

pyroxene of diopside and hedenbergite). However, due to the presence of Na and Al, the necessary elements in a non-quadrilateral pyroxene, AUG actually falls along the Jadeite-Aegirine solid solution. Because AUG is non-standard and contains an array of additional phases, we are unable to find a suitable comparison in published literature. Thus, we expanded our search for suitable comparison to the JPL, JHU, and BED spectral libraries. In particular, we looked at emission and reflectance spectra of augite, jadeite, and additional phases (phlogopite, quartz, enstatite, and hypersthene; see Table 1).

Rather than comparing RB positions, we examine the locations of all $AUG_{SML,0}$ minima (Table 8). As $AUG_{SML,0}$ minima do not *uniquely* correspond to any augite, phlogopite, quartz, or enstatite feature, we focus the comparison on jadeite (NMNH B18463), and hypersthene (NMNH C2368 and hypersthene_180c25_63) from the JHU and BED spectral libraries, recognizing that the $AUG_{SML,0}$ features may be due to a combination of minerals in the AUG mixture. For example, the BED hypersthene spectrum exhibits a series of cascading minima similar to D_4, D_5, and D_6 in $AUG_{SML,0}$, but at slightly different locations, while an enstatite spectrum from Hamilton (2000) (sample NMNH-34669) exhibits a series of cascading minima in positions closer to D_4, D_5, and D_6. As D_2 and D_3 are likely due to hypersthene, and there are no other enstatite features, hypersthene with minor contributions from enstatite in AUG is a potential cause for the cascading shape of D_4, D_5, and D_6.

Though D_1 may be an RB associated with the mineral jadeite (Table 8), it is not easily distinguished in $AUG_{S,0–90}$. In $AUG_{ML,0–90}$ D_1 does not shift in position considerably, so it may be a reasonable indicator of composition if particle sizes are known to be <20 μm. The position of other minima are highly dependent on regolith porosity, and thus are ill suited for compositional analysis. Finally, there are no $AUG_{SML,0–90}$ maxima that we found to correlate to vibrational bands. As such, none of the maxima are good indicators for compositions, regardless of regolith porosity.

4.8. Enstatite + fayalite

4.8.1. Surface scattering dominated spectra

For spectra of low regolith porosity MXT samples, we assign D_3, and D_9 as enstatite RBs, and D_4 and D_8 olivine RBs (Table 9). As the minerals in MXT are roughly equal parts olivine and pyroxene, we compare $MXT_{SML,0}$ to emissivity spectra of enstatite (Mg_{67}; NMNH-B18427) reported in Hamilton (2000) and olivine (Mg_{50}) reported in Lane et al. (2011). As with the numbering scheme for RBs defined in Hamilton (2000), we refer to the Lane et al. (2011) defined bands as 'L_x', with 'x' representing the band number. D_2 could be an enstatite or olivine RB as both H_1 and L_1 are in a similar position, but much deeper than D_2, which could be due to overlapping bands in close proximity to each other.

In the surface scattering-dominant regime, D_3 and D_4 are the best RBs for identifying enstatite and olivine respectively in $MXT_{SML,0}$. While D_2 shifts in position considerably, D_3 and D_4 remain unshifted in all $MXT_{SML,0–90}$ (Fig. 8). In contrast to D_3, D_4 is small and difficult to identify on its own. Therefore, at low regolith porosities, the olivine features are more readily identifiable and the best indicator of overall composition.

In spectra of high regolith porosity samples (i.e., $MXT_{SML,90}$), we identify P_4, P_5, P_7, and P_8 as olivine bands using the olivine ($Mg_{56.8}$) spectrum from Koike et al. (2003), and P_{11} and P_{12} as enstatite bands using the enstatite (Mg_{50}) spectrum from Chihara et al. (2002) (Table 9). The 10-μm region is dominated by olivine bands, but at longer wavelengths, there are fewer olivine maxima, so enstatite bands are unobstructed.

4.8.2. Volume scattering dominated spectra

In the volume scattering-dominant regime, P_8 is the best feature for identifying olivine, while P_{11} is best for enstatite identification in MXT spectra. As P_4-P_8 correspond to olivine vibrational bands at low regolith porosity, their positions are indicative of composition. Interestingly, P_8 is the only maximum identifiable at all regolith porosities, and it does not shift in position in any $MXT_{SML,0–90}$. Furthermore, P_8 corresponds to the feature P_9 from Martin et al. (2022), which was also found to be the best feature for mineral and compositional identification in pure olivine spectra. The enstatite feature, P_{11} does not shift considerably with increasing regolith porosity, yet P_{12} does, and thus may be a poor indicator of composition. The spectral contrast of P_{11} is very low, and may be difficult to distinguish in a spectrum with noise over ~2%. Nonetheless, mineral identification of enstatite + fayalite mixtures is best done using 10-μm region maxima for fayalite and 16-μm region maxima for enstatite.

4.9. Applications to small bodies

Generally, we find that common pyroxenes like enstatite, diopside, and potentially hedenbergite have clear indicators that can be identified by remote sensing, even at high regolith porosity: enstatite maxima that are roughly equal spectral contrast at 9.3 and 10.5 μm followed by a series of small maxima between 13.0 and 15.5 μm; diopside maxima at ~9.3 (prominent), ~14.8, and 15.8 μm; and hedenbergite maxima of equal spectral contrast at ~9.4, 10.4, and 11.5 μm followed by two maxima at ~15 and 16 μm. To distinguish these three minerals, we note that if a maximum at 9.3 μm is the most prominent maximum in the 10-μm region, then diopside is likely present. Otherwise the maximum is either due to enstatite or hedenbergite. Furthermore, if there are small scale features in the ~13–14 μm region, enstatite is likely present rather than hedenbergite. For pyroxene characterization on airless bodies beyond these feature identifications, we recommend performing mixing models that account for particle size and regolith porosity.

As we have noted previously (Martin et al., 2022), our laboratory reflectance spectra, taken under ambient conditions, and emissivity spectra of an airless body, should be prudently compared because environmental effects (pressures, temperatures, and temperature gradients) can potentially alter resulting spectra (e.g., Donaldson Hanna et al., 2017; Donaldson Hanna et al., 2021). Changes in MIR spectra taken in a vacuum environment arise due to steep thermal gradients in the near surface (upper 100 μms; e.g., Henderson and Jakosky, 1997). For example, CFs, which are pure scattering features, can shift in position depending on pressure and thermal environment. However, as discussed in Sections 4.3–4.8, there are also many features consistent with spectra taken under vacuum conditions, which can be used for compositional analysis of asteroid surfaces. In the following, we focus on comparing our laboratory spectra, as well as those of amorphous enstatite, with asteroid (624) Hektor, focusing on the 10-μm plateau region.

The shape of Hektor's 10-μm plateau has been attributed to fine-particulate crystalline and amorphous silicates either making up a

Table 9
Average minima positions that correspond to RBs identified in Hamilton (2000) and Lane et al. (2011), and maxima that correspond to bands in Koike et al. (2003) and Chihara et al. (2002). Bands useful for compositional identification or regolith porosity estimation are underlined. *Indicates a tentative correspondence.

MXT feature	Ave. position (μm)	Cor. band	Cor. band position (μm)
*D_2	9.48 μm	H_1/L_1	9.61/9 μm
$\underline{D_3}$	10.34 μm	H_2	10.31 μm
$\underline{D_4}$	10.82 μm	L_3	10.76 μm
D_8	16.61 μm	L_6	16.92 μm
D_9	18.11 μm	H_6	18.66 μm
P_4	10.14 μm	K_2	10.16 μm
P_5	10.51 μm	K_3	10.64 μm
P_7	11.38 μm	K_4	11.27 μm
$\underline{P_8}$	11.96 μm	K_5	12.00 μm
*P_{10}	13.78 μm	$C_{8/9}$	~13.7 μm
$\underline{P_{11}}$	15.18 μm	C_{10}	14.90 μm
P_{12}	16.68 μm	C_{11}	15.60 μm

highly porous regolith or suspended in a transparent matrix (e.g., Emery et al., 2006; Yang et al., 2013; Martin et al., 2022). The overall lack of high contrast emissivity features (i.e., individual crystalline forsterite bands) has been attributed to the presence of amorphous material (Emery et al., 2006; Vernazza et al., 2012). Though we agree that Trojan surfaces likely have considerable amorphous material, we also argue, based on our porosity experiments, that the overall shape of the 10-μm plateau is largely controlled by regolith porosity (in addition to particle size). In fact, we find good agreement between our laboratory spectrum of crystalline enstatite ($ENS_{S,90}$) and Hektor's emissivity spectrum (Fig. 10), as both have a maximum near ~9.3 μm, the location of $ENS_{S,90}$ P_4, and the overall shape of the 10-μm plateaus is similar. There is a maximum in Hektor's spectrum at ~11.2 μm that has been attributed to olivine (Martin et al., 2022) and a maximum near ~11.7 μm in our $ENS_{S,90}$, corresponding to a weak resonance band, that we do not see in the Hektor spectrum. We suspect that the latter feature may be attenuated by the presence of amorphous material, which we observed in synthetic spectra of amorphous and crystalline enstatite mixtures (Fig. 10). Thus, we suggest that Hektor's surface is covered in a porous regolith of both fine-particulate crystalline and amorphous silicates.

Martin et al. (2022) assessed the regolith porosity of Hektor and concluded that if it were primarily fine-particulate olivine, it would have to have at least 81% void space in the regolith. Following the same argument, we now estimate the total porosity on Hektor's surface assuming it is entirely fine-particulate enstatite. $ENS_{S,0–90}$ tends to lose the CF around 50% regolith porosity, while $ENS_{ML,0–90}$ tends to lose the CF around 70% regolith porosity. The 45–63 μm 70% regolith porosity sample has a *total* simulated porosity of ~88%, as it includes the calculated void space (see Table 2) in addition to 70% KBr. In $ENS_{,S,0–90}$, the CF is lost at ~50% regolith porosity, which is ~84% *total* simulated porosity. Thus, whether considering olivine or pyroxene as the dominant composition, we conclude that the total void space in Hektor's regolith is >80%.

5. Conclusions and future work

As MIR spectral interpretation of airless bodies can be challenging, we aimed to untangle the effects of particle size and porosity to identify minerals at each degree of regolith porosity for eight pyroxene samples over three particle size ranges. Our results presented here show the quantifiable effect regolith porosity has on MIR spectra of pyroxenes and pyroxene-olivine mixtures, consistent with our previous studies on olivine (Martin et al., 2022). Specifically, we find that 0% regolith porosity spectra are dominated by surface scattering, while the 90% regolith porosity spectra are dominated by volume scattering. The transition between scattering regimes is gradual and depends on particle size (i.e., spectra of smaller particles will more readily transition to volume scattering). We previously identified a peak maximum at ~11.0 μm that is indicative of high regolith porosity olivine spectra, but only identified one pyroxene spectral suite ($AEG_{SML,0–90}$) that has a similar feature (P_5 at ~10.9 μm), suggesting that there may not be a universal marker for high regolith porosity in pyroxenes. We also find a number of key features in spectra of aegirine, enstatite, diopside, and hedenbergite that can be used to for their identification on an airless body (i.e., maxima at ~9.3 μm and in the 13–14 μm region), regardless of their porosity.

We compared Hektor's MIR spectrum to modeled mixtures of crystalline and amorphous enstatite as well as to $ENS_{S,90}$. We found that the existence of a 10-μm plateau on an optically thick surface, such as an asteroid, can be indicative of both high porosity regolith and amorphous silicates, and we estimate the regolith porosity of Hektor's surface to be >80%, consistent with Martin et al. (2022).

Though olivine and pyroxene are common minerals found on many extraterrestrial surfaces, it is unlikely for a surface to be entirely made of these two silicate constituents. Thus, in future studies, we plan to explore how the porosity affects the MIR spectra of phyllosilicates and mixtures of additional minerals. Finally, our laboratory measurements were made under ambient environmental conditions. As such, future studies will include conducting measurements in high vacuum, temperature-controlled environments, analogous to asteroid surfaces.

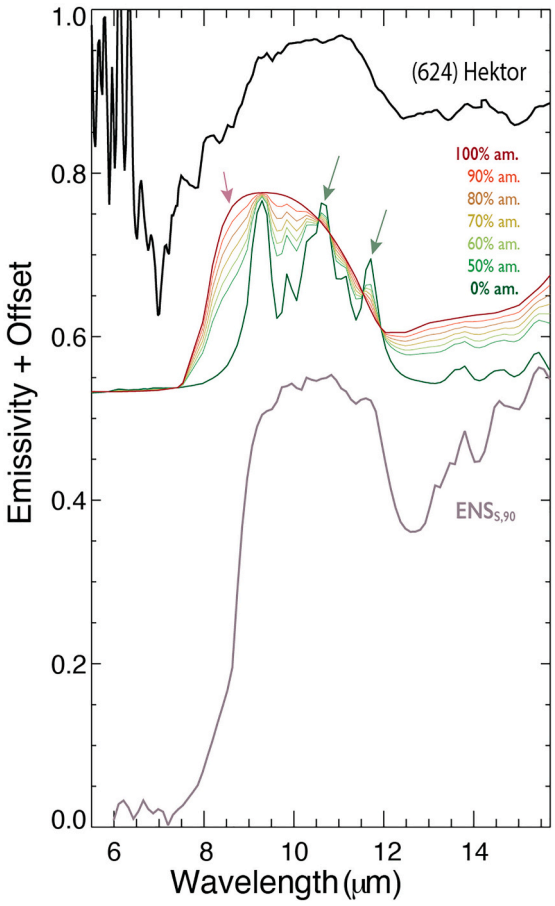

Fig. 10. Spitzer Space Telescope spectrum of (624) Hektor is shown in black (from Emery et al., 2006). $ENS_{S,90}$ is shown in gray, and mixtures of amorphous (am.) and crystalline enstatite are shown in colors ranging from red to green (100% am. in dark red, 0% am. in dark green). Am. pyroxene optical constants come from Dorschner et al. (1995) and are calculated from emissivity equation in Lisse et al. (2006; supplemental) using a particle radius of 5 μm. Crystalline emissivity spectra are from Chihara et al. (2002). All enstatite spectra are binned down to 100 data points between 5 and 16 μm, and the amorphous and crystalline mixture spectra have been multiplied by 0.5 for comparison purposes. Light red arrow points to the 9.1-μm inflection and light green arrows point to the 10.6-μm and 11.7-μm bands. (For interpretation of the references to colour in this figure legend, the reader is referred to the web version of this article.)

Declaration of Competing Interest

The authors declare that they have no known competing financial interests or personal relationships that could have appeared to influence the work reported in this paper.

Data availability

Data are in spreadsheets in 'Attach File' step in .xlsx format. Any additional data will be available upon request.

Acknowledgments

The authors would like to thank Sean Lindsay, Daniel Britt, Will

Grundy, and Carey Lisse for invaluable discussions regarding the inception, and methodology of this work, and Molly McCanta and Allan Patchen for their guidance with electron microprobe sample preparation. Additional thanks goes to the National Museum of Natural History (NMNH) for lending their B06-045 to our study. We would also like to acknowledge that this work was primarily done in Northern Arizona, at the base of the San Francisco Peaks, on homelands sacred to Native Americans through the region. Additional work was done in Eastern Tennessee, on the traditional land of the Tsalagi and Tsoyaha people. This work is supported by the National Aeronautics and Space Administration's Science Mission Directorate Research and Analysis Solar System Workings programNH19ZDA001N.

Appendix A. Supplementary data

Supplementary data to this article can be found online at https://doi.org/10.1016/j.icarus.2023.115507.

References

Chihara, H., et al., 2002. Compositional dependence of infrared absorption spectra of crystalline silicates I. Mg-Fe pyroxenes. Astron. Astrophys. 391, 267–273.
Delaney, J.S., et al., 1984. The polymict eucrites. Proceedings of 15th Lunar Planetary Science Conference. J. Geophys. Res. 89, C251–C288.
Dobrică, E., et al., 2012. Transmission Electron Microscopy of CONCORDIA ultracarbonaceous Antarctic micrometeorites (UCAMMS): mineralogical properties. Geochim. Cosmochim. Acta 76, 68–82.
Donaldson Hanna, K.L., et al., 2017. Effects of varying environmental conditions on emissivity spectra of bulk lunar soils: application to Diviner thermal infrared observations. Icarus 283, 326–342.
Donaldson Hanna, K.L., et al., 2021. Spectral characterization of Bennu analogs using PASCALE: anew experimental set-up for simulating the near-surface conditions of airless bodies. J. Geophys. Res. Planets 126.
Dorschner, J., et al., 1995. Steps toward interstellar silicate mineralogy. II. Study of Mg-Fe- silicate glasses of variable composition. Astron. Astrophys. 300, 503–520.
Dunn, T.L., et al., 2010. Analysis of ordinary chondrites using powder X-ray diffraction: 1. Modal mineral abundances. Meteorit. Planet. Sci. 45, 123–134.
Emery, J.P., et al., 2006. Thermal emission spectroscopy (5.2-38 μm) of three Trojan asteroids with the Spitzer Space Telescope: detection of fine-grained silicates. Icarus 182, 496–512.
Frank, D.R., et al., 2014. Olivine in terminal particles of Stardust aerogel tracks and analogous grains in chondrite matrix. Geochim. Cosmochim. Acta 142, 240–259.
Gail, H.P., 2004. Radial mixing in protoplanetary accretion disks IV. Metamorphosis of the silicate dust complex. Astron. Astrophys. 413, 571–591.
Gastineau-Lyons, H.K., et al., 2002. A critical evaluation of oxidation versus reduction during metamorphism of L and LL group chondrites, and implications for asteroid spectroscopy. Meteorit. Planet. Sci. 37, 75–89.
Hamilton, V.E., 2000. Thermal infrared emission spectroscopy of the pyroxene mineral series. J. Geophys. Res. 105, 9701–9716.
Heiken, G.H., et al., 1991. Lunar Source-Book: A User's Guide to the Moon. Cambridge Univ. Press, New York.
Henderson, B.G., Jakosky, B.M., 1997. Near-surface thermal gradients and mid-IR emission spectra: a new model including scattering and application to real data. J. Geophys. Res. 102 (E3), 6567–6580.
Henning, T., 2010. Cosmic silicates. Annu. Rev. Astron. Astrophys. 48, 21–46.
Izawa, M.R.M., et al., 2021. Salt – a critical material to consider when exploring the solar system. Icarus 359, 114238.
Klima, R.L., et al., 2008. Characterization of the 1.2 μm M1 pyroxene band: extracting cooling history from near-IR spectra of pyroxenes and pyroxene-dominated rocks. Meteorit. Planet. Sci. 43, 1591–1604.
Koike, C., et al., 1993. Extinction of olivine and pyroxene in the mind- and far-infrared. Mon. Not. R. Astron. Soc. 264, 654–658.
Koike, C., et al., 2000. Absorption spectra of Mg-rich Mg-Fe and Ca pyroxenes in the mid- and far-infrared regions. Astron. Astrophys. 363, 1115–1122.
Koike, C., et al., 2003. Compositional dependence of infrared absorption spectra of crystalline silicate II. Natural and synthetic olivines. Astron. Astrophys. 399, 1101–1107.
Lane, M.D., et al., 2011. Midinfrared spectroscopy of synthetic olivines: thermal emission, specular and diffuse reflectance, and attenuated total reflectance studies of forsterite to fayalite. J. Geophys. Res. E Planets 116.
Lisse, C.M., et al., 2006. Spitzer spectral observations of the deep impact ejecta. Science 1979 (313), 635–640.
Martin, A.C., 2022. MID-infrared spectral studies of Jovian Trojan asteroids and the effects of regolith porosity (Publication No. 12445) [Doctoral Dissertation, Northern Arizona University]. ProQuest Dissertations & Theses Global.
Martin, A.C., et al., 2022. Spectral effects of regolith porosity in the mid-IR – Forsteritic olivine. Icarus 378.
Petaev, M.I., Wood, J.A., 1998. The condensation with partial isolation (CWPI) model of condensation in the solar nebula. Meteorit. Planet. Sci. 33, 1123–1137.
Salisbury, J.W., et al., 1991. Midinfrared (2.5-13.5 μm) reflectance spectra of powdered stony meteorites. Icarus 92, 280–297.
Sunshine, J.M., et al., 2004. High-calcium pyroxene as an indicator of igneous differentiation in asteroids and meteorites. Meteorit. Planet. Sci. 39, 1343–1357.
Vernazza, P., et al., 2012. High surface porosity as the origin of emissivity features in asteroid spectra. Icarus 221, 1162–1172.
Wooden, D.H., et al., 2017. Cometary dust: the diversity of primitive refractory grains. Phil. Trans. R. Soc. A Math. Phys. Eng. Sci. 375.
Yang, B., et al., 2013. Are large Trojan asteroids salty? An observational, theoretical, and experimental study. Icarus 223, 359–366.